Appendix I

Appendix I

Journal publications and book chapter details

Papers published

1. Basumatary, R., Basumatary, P., Hazarika, S. J., Konwar, D., & Ramchiary, A. (2025). Advanced LDH-derived Ag@NiO/Ag_2CrO_4 heterojunction photocatalyst for rapid dye degradation. *Journal of Water Process Engineering*, *78*, 108727.
2. Basumatary, R., & Ramchiary, A. (2025). Unveiling the role of anisotropy effects of plasmonic Ag nanostructures in modulating visible light photocatalysis of TiO_2. *Materials Letters*, *40,* 139292.
3. Basumatary, R., Konwar, D., & Ramchiary, A. (2025). Advances in plasmonic photocatalysts for solar light harvesting and enhanced performance: A comprehensive analytical review. *Solar Energy Materials and Solar Cells*, *282*, 113353.
4. Basumatary, R., Konwar, D., Basumatary, B., & Ramchiary, A. (2023). Plasmonic enhanced branched Ag sensitized Cu_2O–CuO/TiO_2 heterojunction with unprecedented photocatalytic degradation under visible light. *Journal of Physics and Chemistry of Solids*, *180,* 111435.
5. Basumatary, R., Basumatary, B., Konwar, D., & Ramchiary, A. (2023). Tailored highly efficient Co-doped TiO_2/$CoTiO_3$ heterojunction photocatalyst for methylene blue degradation under visible light. *Journal of the Korean Ceramic Society*, *60*, 547-559.
6. Basumatary, P., Basumatary, R., Konwar, D., & Ramchiary, A. (2025). Dual type-II heterojunction in $SrTiO_3$/TiO_2/Cu_2O photocatalyst: A robust system for dye degradation under visible light. *Surfaces and Interfaces*, *62*, 106148.
7. Basumatary, B., Basumatary, R., Ramchiary, A., & Konwar, D. (2022). Evaluation of Ag@TiO_2/WO_3 heterojunction photocatalyst for enhanced photocatalytic activity towards methylene blue degradation. *Chemosphere*, *286,* 131848.

Appendix I

Book chapters

1. Basumatary, R., Brahma, S., & Ramchiary, A. (2025). Chapter: Low dimensional metal oxide semiconductors: A promising frontier for biosensing applications, Book: One- and Two- Dimensional Nanomaterials Bioengineering Applications, Academic Press (Elsevier), ISBN: 978-0-443-23703-4
2. Basumatary, R., & Ramchiary, A. (2025). Chapter: Plasmonic metal integrated semiconductor photocatalysis, Book: Frontiers in Natural Sciences, IQAC Birjhora Mahavidyalaya, ISBN: 978-81-96595-47-0
3. Basumatary, R., Basumatary, P., Das H., & Ramchiary, A. (2023). Chapter: Synthesis and enhancement strategies for metal oxide photocatalysts for sustainable energy and environmental challenges, Book: Biological, Chemical and Physical approach to materials and it's applications, National Press Associates, ISBN: 978-81-19674-31-2.

Appendix II

Conferences and workshops

Conferences

1. "Pushing Frontiers: Plasmonic Ag-enhanced Ni-Cr LDH photocatalysts propel swift visible light dye degradation" presented at International Conference on Recent Advances in Mathematical, Physical and Chemical Science (ICRAMPC-2024) organized by School of Physical Sciences, Mizoram University, Aizawl, during February 21 - 23, 2024
2. "Synthesis of various shaped silver (Ag) nanostructures via facile chemical methods: Evaluation of plasmonic characteristics and photocatalytic enhancement" presented at Fourth International Conference on Material Science (ICMS-2024) organized by Department of Physics, Tripura University, during 31st Jan - 2nd Feb 2024
3. "Plasmonic Resonance in coupled plasmonic nanoparticles" presented at 1st Bodoland International Knowledge Festival (BIKF-2023), organized by Bodoland University, Kokrajhar, during 27th Feb – 2nd March 2023
4. "Broad LSPR enhanced CuO/TiO_2 heterojunction photocatalyst for MB degradation" presented at National Conference on Advances in Sustainable Chemistry and Material Science (ASCMS-2022), organized by Department of Chemistry, Bodoland University, Kokrajhar, during 29 - 30th April 2022

Workshops

1. Five day Hands on Training Cum Workshop on “Application of SEM & EDS on Biological Samples” organized by Department of Biotechnology, Bodoland University from 5th to 9th January, 2024.
2. International Workshop on “AI Tools for Research Writing” organized by Manuscriptpedia, Knayakumari, during 6th and 7th January 2024.
3. Training on “Sophisticated Instuments used in Scientific Research” organized by Sophisticated Analytical Instrument Centre (SAIC), Institute of Advanced Study in Science and Technology (IASST), Guwahati during 7 to 13, 2022.
4. Nine days online workshop on “Opportunities for Research and Innovation Using the Facilities of SAIF-Guwahati from 14th to 23rd February 2022.
5. One-day workshop on Building Research Capacity in Physics organized by the Department of Physics, Bodoland University, Kokrajhar, Assam on 15th June 2022.
6. Two days online workshop on “Scanning Electron Microscopy: Technique and its Applications” organized by North East Centre for Biological Sciences and Healthcare Engineering, Inidan Institute of Technology Guwahati, Assam on 29th - 30th July 2021.
7. One week AICTE sponsored online Short Term Training Programme (STTP) on “Emerging Trends in Nanomaterials for Electronic and Optoelectronic Devices” organized by Department of Electronics & Communication Engineering during May 10-15, 2021.

Journal of Water Process Engineering 78 (2025) 108727

Contents lists available at ScienceDirect

Journal of Water Process Engineering

journal homepage: www.elsevier.com/locate/jwpe

Advanced LDH-derived Ag@NiO/Ag_2CrO_4 heterojunction photocatalyst for rapid dye degradation

Rajmoni Basumatary [a], Phulmani Basumatary [a], Saurabh J. Hazarika [b], Dimpul Konwar [c], Anjalu Ramchiary [a,*]

[a] Department of Physics, Bodoland University, Kokrajhar, Assam, 783370, India
[b] Pandit Deendayal Upadhyaya Adarsha Mahavidyalaya, Tulungia, Bongaigaon, Assam, 783383, India
[c] VSB-Technical University of Ostrava, Centre for Energy and Environmental Technologies, Nanotechnology Centre, 17. listopadu 2172/15, Ostrava, 70800, Czech Republic

ARTICLE INFO

Editor: Laura Bulgariu

Keywords:
Visible light active
Plasmonic
Heterojunction system
Photocatalysis
Dye degradation

ABSTRACT

This work unveils a superior plasmonic photocatalyst synthesized through the strategic integration of metallic Ag during Ni—Cr LDH synthesis. The catalyst synthesis involved the formation of modified Ni—Cr LDH, by the incorporation of a metallic Ag solution and subsequent air heat treatment, leading to the in-situ development of the mixed metal oxide Ag@NiO/Ag_2CrO_4 (ANC). The ANC photocatalyst exhibits strong visible-light absorption and suitably positioned band edges, forming a *Z*-scheme heterojunction that facilitates efficient charge transfer and enhances redox reactivity. The efficacy of the photocatalyst was evaluated by the degradation of MB and RhB dye, revealing that the heterojunction photocatalyst outperformed the LDH derived NiO (NC) counterpart by 34 fold and 1.4 fold in MB and RhB degradation, respectively. The improved catalytic performance mainly stems from its efficient harvesting of visible light, and the plasmonic effects, including local surface plasmon resonance (LSPR) and plasmon induced resonant energy transfer (PIRET). The PIRET phenomena enabled by Ag nanoparticles plays a crucial intermediary role in sustaining an efficient *Z*-scheme charge transfer between Ag_2CrO_4 and NiO. The key significance of this study lies in its innovative synthesis strategy, wherein Ni—Cr LDH serves as a transformative precursor, strategically engineered to develop highly active photocatalysts through the incorporation of plasmonic Ag.

1. Introduction

The rapid industrial expansion and intensive natural resource exploitation have become major contributors to the contamination of surface and groundwater, leading to a concerning decline in freshwater availability. Waste released from industries such as textiles, rubber, paper, and plastics continues to impact aquatic ecosystems adversely, posing serious challenges for society as a whole. Semiconductor-based photocatalysis has evolved into a key research focus for their ability to harness sunlight directly, enabling the production of solar energy through pivotal processes like water splitting, CO_2 reduction, pollutant degradation, and antimicrobial application. The pressing need for sustainable and environmentally conscious approaches to treat dye-contaminated wastewater underscores the critical role of advanced oxidation processes (AOPs), particularly photocatalytic systems. This approach enables efficient breakdown and mineralization of various organic pollutants in water by producing highly reactive oxidizing agents [1]. Photocatalytic degradation of contaminants yields non-toxic by-products, mainly CO_2 and H_2O, showcasing it as an effective method for converting hazardous compounds into environmentally safe products. Despite significant progress, research on photocatalyst development remains ongoing, with a continual pursuit of advanced materials that are cost-effective, practical, and highly efficient. Metal oxide-based photocatalysts like TiO_2 and ZnO have proven effective upon modification and have been widely studied to enhance photocatalytic efficiency [2]. Despite their potential, these semiconductors are hindered by a relatively large band gap, which significantly limits their efficiency in harnessing visible light. While elemental doping has successfully adjusted the band gap, the introduced impurity sites often serve as centers for electron-hole recombination, reducing photogenerated carrier lifespan and thus decreasing photocatalytic efficiency [2]. As a consequence, developing visible-light-responsive photocatalysts such as

* Corresponding author.
E-mail address: anjalu1417@buniv.edu.in (A. Ramchiary).

https://doi.org/10.1016/j.jwpe.2025.108727
Received 6 June 2025; Received in revised form 5 September 2025; Accepted 8 September 2025
Available online 12 September 2025

modified LDH, engineered through metal doping or heterojunction formation, along with other mixed metal oxides possessing narrower band gaps is vital for optimizing solar conversion efficiency.

In the pursuit of effective photocatalytic materials, silver-containing compounds, mainly Ag_2WO_4, Ag_2MoO_4, and Ag_2CrO_4 have garnered considerable interest due to their distinctive photosensitivity, which imparts these materials with exceptional light absorption characteristics that facilitate visible light activated catalytic processes [3,4]. Ag_2CrO_4 distinguishes itself among silver-based semiconductors due to its wide absorption range, and efficient photogenerated carrier transfer, which offer a significant advantage in photocatalytic applications. The distinct crystalline structure and electronic configuration of Ag_2CrO_4 facilitates the migration of photo-induced charge carriers, resulting in optimized production of reactive oxygen intermediates [3,5]. Nonetheless, the limited efficiency of unmodified Ag_2CrO_4 catalysts, due to poor photogenerated carrier separation, restricts their vast application [6]. Studies have shown that strategies such as element substitution, morphology tuning, and heterojunction formation can significantly alleviate this issue [5–7]. A study shows that Eu^{3+} doping augments the photocatalytic ability and stability of Ag_2CrO_4 by modifying its band structure, which improves charge separation and supports multiple degradation pathways, significantly boosting its photocatalytic ability under visible light [4]. In their recent work, Gorouhi et al. explored the application of double *Z*-scheme Ag_2CrO_4/Bi_2O_3-KBi_6O_9Br photocatalysts for degrading various organic dye pollutants [8]. Their findings revealed that the double Z-scheme interface between the catalysts drastically enhanced charge separation, thereby boosting overall photocatalytic performance. In a separate study, the $Ag/Ag_2CrO_4/g\text{-}C_3N_4$ catalyst was used to degrade wastewater laden with tetracycline and quinolone compounds [7]. The findings indicated that the mesoporous $g\text{-}C_3N_4$ framework effectively supported Ag and Ag_2CrO_4 nanoparticles, providing additional active sites, while the plasmon resonance effect combined with a synergistic *Z*-scheme heterojunction strategy offered significant advantages within the composite, thereby enhancing the degradation of organic pollutants.

Among various enhancement strategies, two-dimensional (2D) nanostructures, commonly used as co-catalysts with semiconductor photocatalysts, significantly boost photocatalytic efficiency [9]. Purposeful optimization of tailored photocatalyst structures and surface properties has proven to be a powerful approach for advancing oxidation reactions in photocatalysis. Layered double hydroxides (LDHs) are emerging as an attractive group of 2D structure for solar energy conversion, driven by their distinctive physicochemical properties, including a modifiable layered architecture, compositional adaptability, tunable band gaps, advantages from oxygen vacancies, facile synthetic routes, and low production costs [10,11].

LDHs constitute a family of anionic clay minerals featuring alternating layers of mixed-valent metal hydroxides and charge-compensating interlayer anions. These materials, isostructural with naturally occurring hydrotalcite, contain both divalent (M^{2+}) and trivalent (M^{3+}) cations in their brucite-like layers, with interstitial anions maintaining charge neutrality [12,13]. Because of its 2D layered structure, LDH materials have charge transport properties highly suitable for photo- and electro-catalysis [13]. The lamellar structure of LDH is known to collapse upon calcination, yielding thermally stable mixed oxide phases [12]. However, when the collapsed LDH gets into contact with abundant surrounding moisture in the environment, the former lamellar structure is regained. This memory effect of the LDH is advantageous, as it may facilitate the adsorption of dye or water molecules within the interlamellar spaces, thereby providing additional active sites for oxidation and reduction reactions to occur. Other attractive properties of LDHs are including facile anion exchange, exceptional anion uptake capacity, straightforward synthesis process, and, economic production feasibility. However, the use of LDHs as photocatalysts is still not very popular because of their low efficiency, although their light absorption range is wider as compared to photocatalysts like TiO_2.

Our research demonstrates a novel plasmonic-based photocatalyst developed through the integration of Ag metal onto Ni—Cr LDH, highlighting its photocatalytic efficiency and comprehensive characterization. The synthesis steps of pristine Ni—Cr LDH was followed, until, at a specific stage, incorporation of an Ag metallic solution was performed, yielding a slurry product having brownish color, different from greenish slurry obtained during synthesis of pristine Ni—Cr LDH. The calcination of this modified Ni—Cr LDH at 600^{o} C produced a mixed metal oxide system $Ag@NiO/Ag_2CrO_4$. The $Ag@NiO/Ag_2CrO_4$ photocatalyst exhibit a strong visible light absorption, particularly with plasmonic resonance peak corresponding to an energy of ~2.7 eV. Moreover, its favorably aligned band edges for redox reactions with a *Z*-scheme configuration, facilitate efficient photocatalytic transformation reactions. NiO is a wide band gap p-type semiconductor whose bandgap values lies between 3.0 and 4 eV depending upon the synthesis method employed [14]. On the other hand, Ag_2CrO_4 is a narrow band gap n-type semiconductor with bandgap typically ranging from 1.7 eV to 1.8 eV [5]. However, the composite involving heterojunction between NiO and Ag_2CrO_4 would facilitate p-n junction formation that is expected to benefit from the synergy of high reduction power of NiO due to its conduction band edge position located at energy values more negative than the water reduction level, and strong visible light response of Ag_2CrO_4. The composite is expected to have an improved stability than Ag_2CrO_4 alone and better visible light absorption than NiO alone. Additionally, we found that the presence of Ag in the resultant photocatalyst $Ag@NiO/Ag_2CrO_4$ further benefits the composite via surface plasmon resonance mediated *Z*-scheme charge transfer. The reaction kinetics analysis of MB and RhB degradation indicated 34 and 1.4 times more efficient, respectively, compared to the pristine NC counterpart. The improved photocatalytic ability is ascribed to the key factors: (i) the strong visible light response and effective dye molecule adsorption by the lamellar structure of the ANC composite, (ii) The plasmon induced resonant energy transfer (PIRET) occurrence in the ANC photocatalyst enables efficient charge pair generation in NiO driven by nonradiative resonant energy transfer from Ag nanoparticles, extending charge carrier excitation beyond direct optical transitions and enhancing photocatalytic activity, and (iii) the presence of NiO along with traces of $Ni(OH)_2$, serves as a cocatalyst, effectively enhancing the segregation of photoexcited carriers and stimulating the production of active radicals for photocatalytic reactions. Thus, the synergistic effects of Ag-induced plasmonic resonance, combined with the Ag_2CrO_4/NiO composite structure represents a significant advancement in photocatalytic materials design for the efficient degradation of complex dye molecules.

2. Experimental procedure

2.1. Chemicals applied

$Ni(NO_3)_2.6H_2O$ was supplied by Merck, India. $Cr(NO_3)_3.9H_2O$, 97 % purity, and $Na_2CrO_4.4H_2O$, 99 % were received from Loba Chemie Pvt. Ltd. Sodium Hydroxide (NaOH) was purchased from Avantor Performance Materials India Ltd. Polyvinyl Pyrolidone (PVP) from Himedia Laboratories Pvt. Ltd., India. Sodium Carbonate Anhydrous (Na_2CO_3), Tri-sodium Citrate Dihydrate (TSC, $C_6H_5Na_3O_7.2H_2O$), and Sodium Borohydrate ($NaBH_4$) were obtained from Merck Life Science Pvt. Ltd. $AgNO_3$, and Hydrogen Peroxide (H_2O_2) were provided by Th. Fish. Sci. India Pvt. Ltd.

2.2. Catalyst synthesis protocol

2.2.1. One pot synthesis of Ag solution

The Ag nanoparticle colloidal suspension was prepared in the following steps. To initiate the procedure, 50 mL of doubly distilled (DD) water was used to prepare a solution containing 0.0703 g of silver nitrate ($AgNO_3$). 1.5 mL of PVP solution was added to it by stirring followed by 1.5 mL of TSC. Next, 60 μL H_2O_2 was introduced as an etching agent in

the solution by using a micropipette. After a while, the silver ions in the mixture were finally reduced to silver metal particles under the introduction of 9 mL $NaBH_4$ solution which was done by adding 1 mL aliquots after every 2 s to the mixture.

2.2.2. Preparation of Ni—Cr LDH and Ag@NiO/Ag_2CrO_4

Ni—Cr LDH was prepared by using 0.02 M and 0.01 M of nitrate salts as Ni and Cr precursors respectively in 100 mL DD water. After ensuring the proper mixing of precursors by continuous stirring, 100 mL of 0.01 M $NaCO_3$ was introduced in 1 mL aliquots to the reaction mixture under vigorous stirring. A few moments after the addition of $NaCO_3$, 100 mL of NaOH (1 M) solution, was introduced dropwise to the homogeneous solution. This homogeneous solution was allowed 16 h of thermal aging at 65 °C with mechanical stirring, and finally, the pH was carefully adjusted to 7–8 using DD water. The suspension was filtered, and the collected solids were dried, ground, and calcined at 600 °C.

Preparation of Ag@NiO/Ag_2CrO_4 follows the exact procedures as adopted in the synthesis of Ni—Cr LDH up to the addition of $NaCO_3$ solution. Subsequently, a pre-prepared Ag colloidal suspension was introduced to the suspension, and after 15 min, NaOH solution was subsequently added. All the subsequent steps, as outlined in the Ni—Cr LDH synthesis, were then followed. Subsequently, the formed solid was separated, dried, finely ground into powder, and calcined at 600^0C. The products obtained after calcination at 600 °C are designated as NC for Ni—Cr LDH and ANC for Ag@NiO/Ag_2CrO_4.

2.2.3. Synthesis of Ag_2CrO_4 (AC) counterpart

To prepare Ag_2CrO_4 catalyst, 0.2323 g of $Na_2CrO_4.4H_2O$ was dispersed in 50 mL doubly distilled water which developed into a yellowish solution. Meanwhile, the $AgNO_3$ solution was separately prepared by mixing 0.0516 g of $AgNO_3$ in 50 mL DD water. While putting the chromate salt solution under vigorous stirring, the silver nitrate solution was added dropwise onto it, causing the mixture to gradually turn reddish as the drops were introduced. The mixture was subjected to uninterrupted agitation for a further duration of two hours after which the precipitate was collected, thoroughly washed, and dried.

2.3. Analytical techniques

The XRD data of the powdered photocatalysts were obtained using Bruker-D8-AXS Advance X-ray diffractometer, Cu Kα radiation, $\lambda = 1.54$ Å. The inner structure, morphology, and elemental composition along with its distribution was investigated by using Scanning Electron Microscopy (SEM, Hitachi S4200) and Transmission Electron Microscopy (TEM, FEI Tecnai G2 F20, JEM-2100 PLUS (HR), Jeol) aided with EDX. The UV-DRS spectra were recorded by the Shimadzu UV-1800 machine. To interpret the surface oxidation states and chemical arrangements of the final composite, X-ray photoelectron spectroscopy (K-Alpha X-ray XPS, Thermo 125 Scientific, UK) was employed. Raman shift was examined with a Renishaw basis series Raman Spectrophotometer (514 nm lasers). The photoluminescence (PL) data of the samples were obtained using a PL spectrophotometer (FluoroMax-4C; 1379D, UK). Time-resolved photoluminescence spectra (TRPL) were obtained from Picosecond lifetime spectrophotometer, model: Lifespec II, Edinberg Instruments.

2.4. Photocatalytic assessment for MB and RhB degradation

The effectiveness of the prepared photocatalysts in catalyzing dye degradation was investigated using a light source ($\lambda > 400$ nm; visible irradiance = 4.6 mW/cm^2) as a visible light source and MB and RhB dye as the model pollutant. Throughout the experiments, 0.5 gL^{-1} catalyst loading and 0.01 mM MB and RhB solution were maintained. The sorption equilibrium of the catalyst was established prior to light irradiation. An adequate amount of liquid sample was then collected from the solution under light illumination at every 15-minute interval. Optical absorption profiles of the treated dye were acquired using a double-beam spectrophotometer (make: Shimadzu, model: UV1900i).

2.5. Free radical identification test

The pollutants degradation using photocatalyst is a surface driven phenomenon that intimately involves reaction of adsorbed pollutant molecules with the generated ROS. The contribution of these active species; mainly electrons (e^-), holes (h^+), hydroxyl radicals (•OH), superoxide radicals ($\bullet O_2^-$), and singlet oxygen ($^1O_2$) in degradation process, was examined using selective quenching agents as follows: silver nitrate (SN) for e^-, ammonium oxalate (AO) for h^+, p-benzoquinone (BQ) for $\bullet O_2^-$, isopropyl alcohol (IPA) for •OH, and L-histidine (LH) for $^1O_2$ [15–17]. The experiment was performed following the same procedures as described in the photocatalytic degradation experiment using the same MB concentration, catalyst loading, and time intervals of sample collection.

3. Results and discussion

3.1. Crystallographic and optical study

Fig. 1. presents the XRD results of the mixed-metal oxides NC, AC and ANC. The XRD pattern of NC (Ni—Cr LDH calcined at 600 °C) exhibits distinct peaks at 2θ values of 37.1°, 43.6°, and 63.4°, which are attributed to the NiO-like phase, as referenced by JCPDS card no. 04–0835. These reflections are attributable to specific crystallographic planes (111), (200), and (220), respectively [18,19]. Similar types of broad peaks are also observed in ANC at the same 2θ positions, indicative of the same changes that took place after the calcination of raw Ni—Cr layered double hydroxides to form NC and ANC [18,19]. The crystalline phases of LDH and Ag@Ni-Cr LDH in its pristine form were identified through XRD, and are provided in Fig. S1 (supplementary information, SI). Moreover, there are peaks in ANC whose positions coincide with the peak positions of AC (as prepared Ag_2CrO_4) at $2\theta = 17.3^0$, 21.5^0, 25.1^0, 31.1^0, 32.1^0, 33.4^0, 39.1^0, 44.1^0, 45.1^0, 47.8^0, 52.0^0, 55.8^0, 56.8^0, 61.7^0, and 62.4^0. These peaks are identified as representing the XRD pattern of Ag_2CrO_4 (PDF no: 026–0952) [20]. The corresponding planes are (020), (120), (200), (031), (002), (012), (122), (240]. (222), (051), (400), (242), (213), (431), and (402), respectively. The mean crystallite dimensions were calculated to be ~3.6 nm, ~16.1 nm, and ~29 nm for NC, AC, and ANC, respectively, from the Debye-Scherrer formula [21].

The recorded UV–Vis DRS profiles of the photocatalysts NC, AC, and ANC and the UV–Vis absorbance spectra of Ag are plotted in Fig. 2(a). Ag spectrum exhibits two broad spectral features, located at 400 nm and 553 nm. The lower wavelength peak at 400 nm, is interpreted to be primarily resulting from the plasmonic resonance effect associated with the spherical geometry of Ag nanoparticles [22], and another broader peak at 553 nm, was associated to plasmonic resonances arising from Ag nanoparticles of various sizes and shapes, including triangular nanoplates, oblate structures, and irregular forms, as observed in the TEM images in Fig. S2 of SI. The presence of plasmonic Ag in the ANC sample is evident from the distinct bump at 400 nm in the absorption spectrum, indicating its characteristic plasmonic resonance. Additionally, the NC spectra exhibit an increasing absorption trend with decreasing wavelength across the visible-to-UV spectrum (550–300 nm). Similarly, there is an increasingly higher absorption in ANC below 550 nm and beyond 300 nm towards the UV region. This similar absorption trend of NC and ANC can be attributed to their common LDH phase. The optical band gap energies of the catalysts were estimated using Tauc plot extrapolation derived from the Kubelka–Munk function, as illustrated in Fig. 2(b) [23]. The values were noted as 3.14 eV for both NC and ANC, and 1.77 eV for AC. The obtained band gap value 3.14 eV for NC and ANC aligns with the calculated energy gap of NiO, as shown in Fig. S3. Tauc analysis serve as a standard technique to identify energy gap in semiconductors by displaying a linear region corresponding to direct or indirect band gap

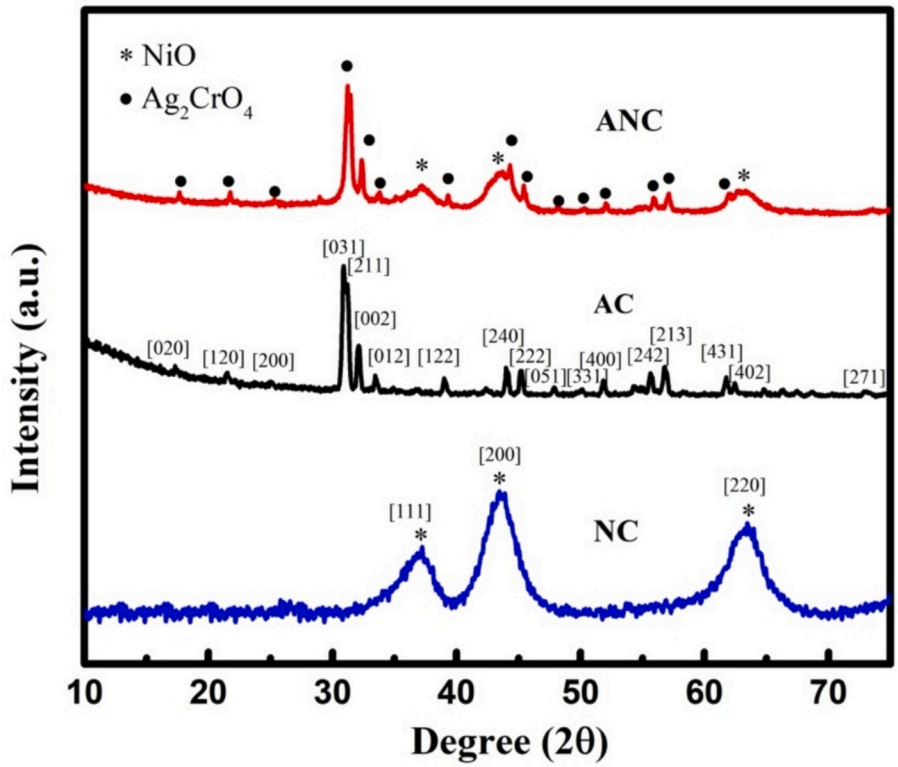

Fig. 1. X-ray diffraction spectra of NC, AC, and ANC.

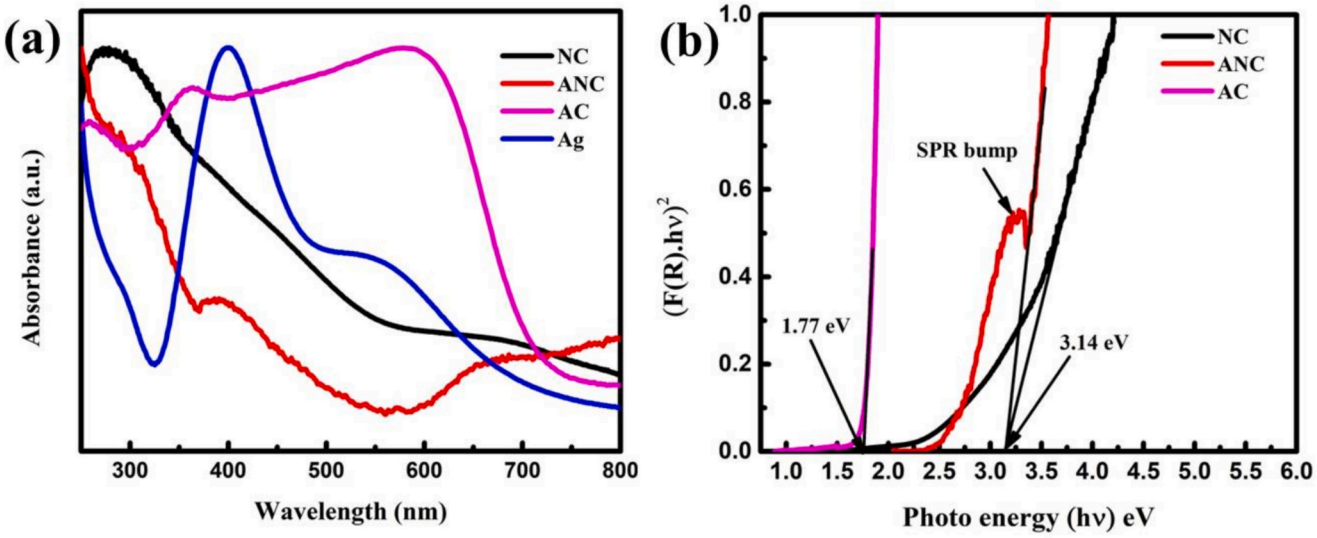

Fig. 2. (a) UV–Vis DRS of NC, AC, ANC, and UV–Vis absorbance spectrum of Ag. (b) Bandgap determination using Tauc plot.

transitions. However, in the presence of Ag nanoparticles, an additional feature can emerge due to the SPR (Surface Plasmon Resonance) effect. The ANC spectrum, reveals a distinct bump starting at around 2.7 eV and having a spectral maximum at 3.1 eV, implying the onset of significant absorption attributed to the SPR of Ag nanoparticles. Although SPR in Ag does not create a true band gap, it can influence the optical properties in a manner that may resemble band gap behavior [24]. This phenomenon can be interpreted as the plasmonic resonance occurring in Ag when the incident light energy surpasses 2.7 eV, aligning with the broad absorption peak of Ag centered at approximately 400 nm (3.1 eV).

3.2. Study of Raman and photoluminescence spectra

Fig. 3(a). presents the Raman shift patterns of the photocatalysts NC, AC, and ANC. The peaks at 362, 598, and 798 cm^{-1} visible in the NC sample are clearly attributed to the formation of spinel $NiCr_2O_4$ [25,26]. Particularly, the intense and asymmetrical band (here with maxima at 798 cm^{-1}) is referenced to the symmetrical stretching mode of the $[CrO_4]$ tetrahedron [27]. It has been explained that this anti-symmetrical elongation vibration is what contributes to the asymmetry of this band. As illustrated in Fig. 3(a), the Raman analysis of ANC and pristine Ag_2CrO_4 (AC) exhibit nearly identical patterns. Prominent

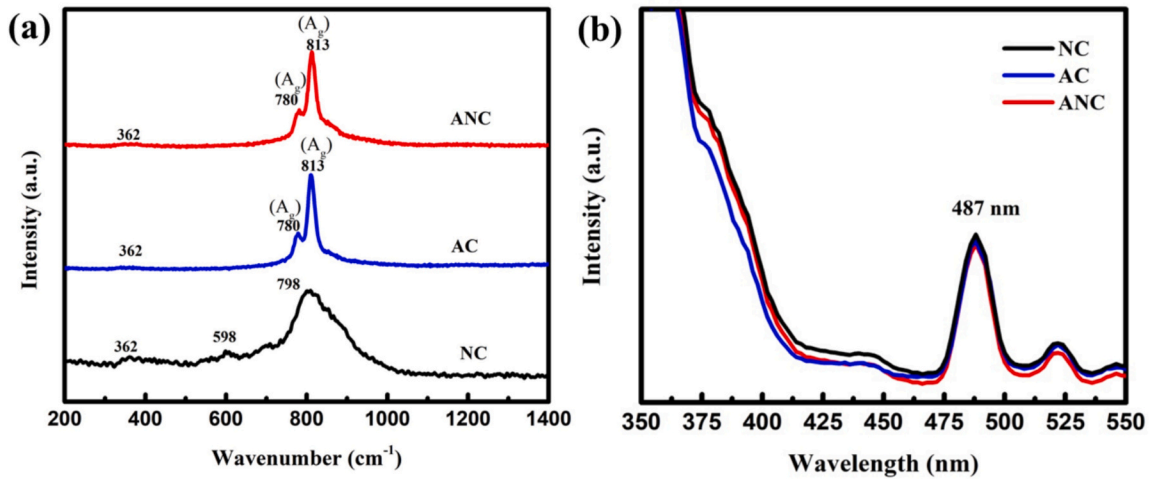

Fig. 3. (a) Raman and (b) Photoluminescence spectra of NC, AC, and ANC.

peaks detected at 780 and 813 cm^{-1} are ascribed to the symmetric vibrational modes of Cr—O bonds within [CrO_4] clusters, corresponding to A_g mode [5,28]. A slight displacement of the peak from 816 cm^{-1} (reported elsewhere) to 813 cm^{-1} was observed, which can arise from the differences in synthesis method, crystallite size, defects in the lattice, and other factors [28]. All the samples (NC, AC, and ANC) have shown a common peak at 362 cm^{-1}, which can be accredited to Cr^{6+}, as all the samples contain Cr and O as their constituent elements [29].

The photoluminescence (PL) spectra of the catalysts NC, AC, and ANC were recorded under 325 nm excitation, as shown in Fig. 3(b). All the photocatalysts displayed minimal emissions in the 400–550 nm wavelength range. Furthermore, ANC shows lower emission than both AC and NC within the wavelength range 450 nm to 550 nm as shown in Fig. 3(b). The formation of a heterojunction between Ag_2CrO_4 and NiO in ANC, alongside a Schottky junction with metallic Ag, may lead to faster and higher electron-hole pair separation efficiency [30]. A peak at 487 nm was observed for both NC and ANC, which could be attributed to the NiO phase present in these samples [31,32]. Similarly, a peak at 487 nm was observed for AC caused by the recombination of charge carriers due to the defects in the structure of Ag_2CrO_4 [5].

3.3. XPS analysis

XPS analysis was conducted to probe the surface chemistry and valence states of elements present in the final ANC catalyst. As presented in Fig. S4, the broad survey spectrum of ANC reveals the presence of characteristic peaks corresponding to Ni 2p, Cr 2p, O 1s, Ag 3d, and C 1s. The C 1s peak detected at a binding energy of 284.8 eV is indicative of

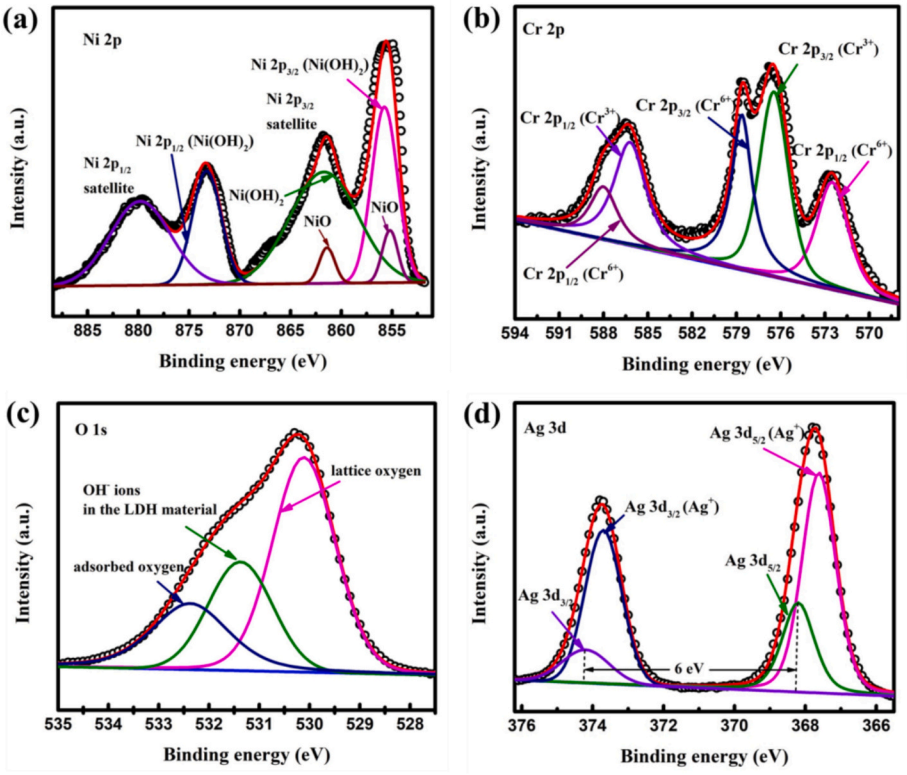

Fig. 4. XPS peak fitting of ANC: (a) Ni 2p spectra, (b) Cr 2p, (c) O 1 s, and (d) Ag 3d.

adventitious carbon contamination on the sample surface [21].

The well-resolved Ni 2p spectrum of ANC is presented in Fig. 4(a). The deconvolution of the Ni 2p spectrum results in six discrete peaks. The main peaks located at 855.7 and 873.2 eV associated with Ni $2p_{3/2}$ and Ni $2p_{1/2}$ doublets, respectively, are identified as the characteristic peaks of $Ni(OH)_2$ [33,34]. The difference in energy of these two peaks matches with the spin-energy splitting value of 17.5 eV, characteristics of a $Ni(OH)_2$ phase [35]. Satellite features at 861.7 eV and 879.8 eV, assigned to $2p_{3/2}$ and Ni $2p_{1/2}$ of $Ni(OH)_2$, provide additional evidence for its existence [36]. While XRD analysis of the ANC material detected NiO-like crystalline phases, XPS revealed additional $Ni(OH)_2$ signatures. This is probably a consequence of the structural breakdown of the LDH layered structure [12]. Under these circumstances, the intercalated anions and bonded hydroxyl molecules in ANC were completely removed after calcination. When exposed to water in the atmosphere and environmental anions such as during the time interval after calcination and before XPS analysis, the LDH likely reformed its former stratified structure with new guest anions or hydroxyl ions, leading to the presence of $Ni(OH)_2$ [12]. Moreover, since XPS is a surface analysis technique, the $Ni(OH)_2$ peaks are found to be predominant [37]. As for the existence of NiO, two characteristic Ni $2p_{3/2}$ peaks at 855.2 eV and 861.4 eV appear with a considerably smaller peak area, in agreement with XRD peaks [36]. In summary, analysis of the Ni 2p spectrum confirms only a single oxidation state, Ni^{2+}, present either as NiO or $Ni(OH)_2$.

Fig. 4(b) depicts the core-level Cr 2p XPS measurement of ANC. The peak maxima recorded at 576.5 eV and 586.2 eV can be associated with Cr^{3+} [18,38,39]. The finding of Cr^{3+} agrees with the general formula of Ni—Cr LDH, in which one metal, Ni is in +2 oxidation state and the other metal, Cr, is in +3 oxidation state. However, the XRD of ANC also revealed the presence of the Ag_2CrO_4 phase, where Cr is in the +6 oxidation state. This is further confirmed by the resolved peaks at 578.6 eV and 588.0 eV in the Cr 2p spectra, corresponding to Cr^{6+} [40]. The additional peak identified at 572.5 eV can be linked to the interplay between Ag 3p and Cr 2p and is referenced as the Ag $3p_{3/2}$ peak [41,42].

The O1s spectra as provided in Fig. 4(c) could be resolved into three district peaks positioned at 530.1 eV, 531.4 eV, and 532.3 eV, which implies the lattice oxygen (Ni—O or Cr—O), hydroxyl oxygen (OH^- ions in the LDH material) and adsorbed oxygen, respectively [33,36,43]. Again, the fine XPS binding energy spectrum corresponding to Ag 3d in the ANC photocatalyst is illustrated in Fig. 4(d). The deconvoluted XPS peaks at 367.6 eV and 373.6 eV are associated with the Ag^+ oxidation state, which supports the formation of Ag_2CrO_4 as revealed in XRD and Cr 2p peaks [40,44]. Furthermore, the Ag 3d doublet, revealed by peaks at 368.2 eV and 374.2 eV corresponding to the $3d_{5/2}$ and $3d_{3/2}$ levels respectively, with a spin-orbit splitting of 6.0 eV, confirms metallic silver presence [21,45]. Fig. S5 presents the valence band XPS spectra, which were utilized to evaluate the band edge positions of the ANC catalyst. Extrapolation at the onset of the spectra, as given in Fig. S5, reveals a valence band maximum (VBM) of 1.26 eV.

3.4. Microstructural investigation of the catalyst

The SEM images of NC exhibit a highly aggregated, porous morphology with nanoparticle clusters forming interconnected structures, shown in Fig. S6(a-b). While a distinct layer-by-layer arrangement is not explicitly visible, the observed agglomerates and rough texture suggest the possible retention of interlayer porosity, a characteristic feature of LDH-derived materials. This porous architecture contributes to a high surface area, which may enhance dye adsorption, offering substantial active sites for photocatalytic reactions [46–48].

In contrast, ANC as displayed in Fig. S6(c-d) display fused layers, implying that the formation and growth of Ag_2CrO_4 have bridged gaps and reduced the height disparity between the uppermost and lowermost surfaces. The stacked and textured appearance observed in the SEM image suggests the presence of residual LDH structures, indicating the retention of its layered morphology in the ANC composite.

To get a detailed information on the morphology of the catalyst, TEM images were investigated. The TEM micrographs of NC are illustrated in Fig. 5(a–d), offer a more detailed observational view of the material's structure. Besides confirming the layered arrangements, the images reveal a mesoporous structure, as observed in Fig. 5(a-b). The TEM image in Fig. 5(c) displays a distinct rod-shaped crystal, identified as NiO [49]. Furthermore, Fig. 5(d) indicates that NC forms a circular structure, which appears to be encapsulated and wrapped with particles, forming the structures as shown in Fig. 5 (a-c).

The TEM images of ANC are presented in Fig. 6(a–c), while the corresponding SAED pattern is shown in Fig. 6(d). It is apparent that ANC is a less porous material with increased crystallinity. Faceted NiO crystal and spherical Ag_2CrO_4 crystals are visible in Fig. 6(b) and (c) respectively [5,49]. The measurement of the radius of concentric circles (highlighted with the red color dotted curve) of the SAED pattern image in Fig. 6(d) reveals four interplanar spacings measured in nanometers (nm) as 0.28, 0.21, 0.18 and 0.13, which are assigned to planes (031), (111), (331) and (271) respectively. The planes (031), (331), and (271) correspond to the growth planes of Ag_2CrO_4 in three different directions while (111) corresponds to the crystal plane of Ag. High-resolution TEM pictures of ANC are presented in Fig. 6(e-f). The measurements of interplanar distances confirm the presence of three distinct phases in ANC, which are Ag, NiO, and Ag_2CrO_4. From the HR-TEM images, in Fig. 6(e), two distinct spacings of NiO are identified at $d = 0.24$ nm and 0.20 nm, corresponding to the [222] and [400] planes, respectively. In addition, Ag_2CrO_4 exhibits an interplanar spacing of $d = 0.28$ nm corresponding to the [031] plane, while metallic Ag shows a spacing of $d = 0.23$ nm corresponding to the [111] plane. Fig. 6(f) further shows distinct spherical Ag nanoparticles of various sizes between the diameter range of 5–11 nm. The EDX analysis of both NC and ANC provides further confirmation of the atomic constituents of these materials. The analysis, as displayed in Fig. S7 of the SI, highlights the existence of elemental components, verifying the successful incorporation of the desired components within the synthesized samples.

3.5. Assessment of photocatalytic performance

The photocatalytic ability of the photocatalysts was determined by tracking the breakdown of MB and RhB molecules. Fig. 7(a-b) demonstrates the degradation trend of MB exposed to visible light for 90 min. The degradation percentage from highest to lowest follows the sequence: ANC > AC > NC with values of 94.6 %, 88.3 %, and 11 %, respectively. The time-resolved UV–Vis absorption spectra of MB, obtained during the experiment using different catalysts, are presented in Fig. S8(a-c). Corresponding photographic images, captured at 15-min intervals are also presented in Fig. S9. The apparent rate constants for MB removal, obtained through linear fits of the ln C/C_o versus time plots (Fig. 7(b)), were determined to be 0.034, 0.025, and 0.001 min^{-1} for ANC, AC, and NC, respectively. The degradation was in accordance with pseudo-first-order kinetics, exhibiting a high R^2 value (0.98, 0.99, 0.86). The degradation rate obtained for ANC photocatalyst is 34 times higher than the pristine NC. The retention of the lamellar LDH structure in ANC, as evidenced by SEM images and XPS spectra, even after forming the heterojunction between NiO and Ag_2CrO_4, offers abundant active sites and facilitates efficient charge carrier separation. Furthermore, $Ni(OH)_2$ with its strong electronegativity, suppresses photogenerated carrier recombination, while combining NiO with $Ni(OH)_2$ aids in the separation of photo-stimulated charge carriers and generates active species for photocatalytic reactions [50]. The Ag_2CrO_4 catalyst also demonstrates effective MB degradation on its own, ascribed to the material's effective visible-light harvesting capability and proficient photogeneration of charge carriers [3]. Furthermore, Ag nanoparticles in metallic form, acts as a plasmonic sensitizer which can improve the visible light response of the semiconductors, as evidenced in the UV-DRS spectra. With the creation of a metal–semiconductor interface (Schottky-type) between

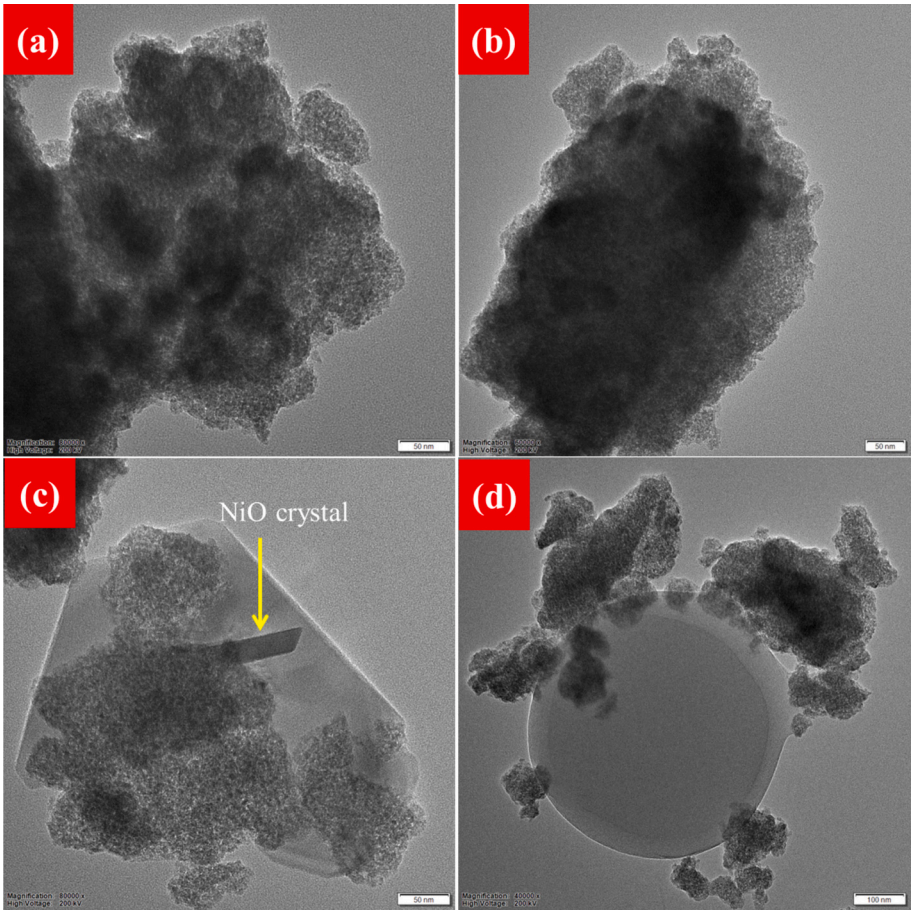

Fig. 5. TEM images of (a–d) NC.

metallic Ag nanoparticles and semiconductor domains, electrons seamlessly transfer from Ag, which serves as both an electron reservoir and a catalytic centre. This process accelerates electron migration while effectively suppressing carrier recombination, thereby enhancing charge separation efficiency. Table S1 presents the rate constants computed for MB degradation of all the photocatalysts along with their regression coefficients from the linear fitting. The photocatalytic degradation of MB is also confirmed from the GCMS analysis results shown in Figs. S10-S12 and Table S2. The GCMS analysis of the degradation products obtained after 90 min of irradiation of MB solution using ANC as the photocatalyst, has been performed. The degradation pathway of MB is presented in Fig. S12. Additionally, rhodamine B (RhB) degradation was performed with the photocatalysts under identical experimental conditions and light exposure. The degradation spectra of RhB are illustrated in Fig. S13(a-b) in SI. The analysis demonstrated that the ANC photocatalyst demonstrated 1.4 times greater activity than NC, the pristine LDH calcined at 600 °C as illustrated in Fig. 7(c-d). The weaker performance of ANC in terms of RhB degradation could be inferred from the role of radicals in RhB degradation. RhB is a dye molecule of molecular weight 479.01 g/mol which is higher compared to that of MB (319.85 g/mol). The degradation mechanism of RhB has been widely studied, and it is accepted that both h^+ and •OH holds a crucial role in enhancing the breakdown of RhB molecules [51,52]. At the first stage of degradation, two competitive process are said to occur simultaneously, namely N-deethylation and chromophore cleavage [52,53]. The cleavage is an important step towards full degradation of RhB whereby it is converted to CO_2 and H_2O. The radicals that are mainly responsible for this cleavage have been identified as h^+, and •OH [52,53]. The •OH that can be obtained from oxidation of H_2O molecules by h^+, require a redox potential of 2.3 eV [54] which is not probable according to the band edge potentials of ANC proposed in this study. However, the production of •OH in ANC photocatalytic system could occur from the participation of electrons in various oxidation reactions via oxygen and water molecules [54]. But accordingly, the population of •OH would be less abundant and thus accounting for slower degradation rate. For MB, the electrons and singlet oxygen are capable enough to degrade MB and thus faster degradation for MB [21]. A comparative summary of the photocatalytic performance of similar composite photocatalysts is presented in Table S3. Furthermore, the reusability test of MB degradation using ANC photocatalyst was performed under the similar experimental set-up for three consecutive cycles as shown in Fig. S14. The total MB removal percentages achieved in three consecutive cycles are 97 %, 81 % and 68 %, respectively. The stability of the photocatalyst was studied by analyzing the obtained XRD spectrum of the ANC photocatalyst subjected to the three cycles of photocatalytic experiment as shown in Fig. S15. Additionally, the supernatant of the degraded MB solution obtained after photocatalysis was examined under UV–Vis spectrophotometer shown in Fig. S16.

3.6. Scavenger-based radical identification experiments

To examine the participating active species and their degree of influence in the degradation of MB using the ANC photocatalyst, free radical quenching experiments were conducted. It is known that photocatalytic process proceed via the major reactions as outlined in Eqs. (1)–(9) [17,55]. Fig. 8(a) shows the degradation of MB using different quenching agents over the course of 90 min. It was found that the addition of LH ($^1O_2$ quencher) to the MB solution lowered the degradation ability of the photocatalyst to a maximum degree in comparison to all other quenching agents tested. The degradation percentages of MB

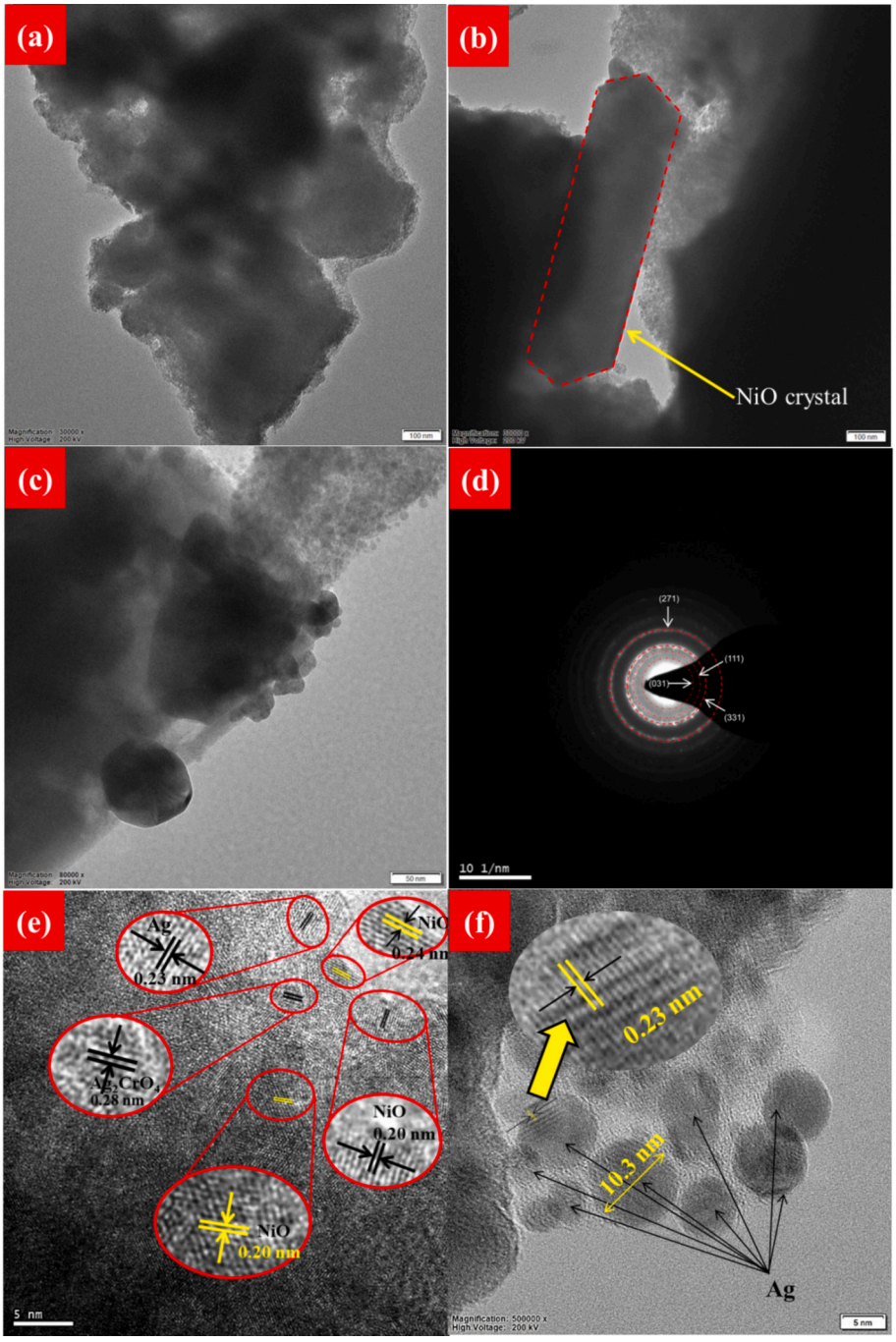

Fig. 6. TEM images of (a–c) ANC, (d) SAED pattern of ANC, and High resolution-TEM images of (e–f) ANC.

after the addition of specific quenching agents are shown in Fig. 8(b). Experimental observations indicated that the presence of BQ ($\bullet O_2^-$ quencher) and SN (e^- quencher) in the MB solution produced second and third highest reduction in degradation efficiency respectively. This observation suggests that electrons (e^-) play a more significant role than holes (h^+) in the degradation of MB using the ANC photocatalyst. This can be explained by the reaction pathways described in Eqs. (2) and (9), where e^- reduces O_2 to form $\bullet O_2^-$, and $\bullet O_2^-$ subsequently interacts with h^+ to generate $^1O_2$. Therefore, when e^- is quenched, $\bullet O_2^-$ production is hindered and the reduced $\bullet O_2^-$ level impairs the generation of $^1O_2$ species, which is the primary reactive species responsible for MB degradation in the ANC photocatalyst system. In contrast, addition of AO (h^+ quencher) and IPA ($\bullet$OH quencher) had a minimal effect on MB degradation as shown in Fig. 8(b).

$$Photocatalyst + h\nu \rightarrow h^+ + e^- \quad (1)$$

$$e^- + O_2 \rightarrow O_2^{\bullet -} \quad (2)$$

$$e^- + O_2^{\bullet -} + 2H^+ \rightarrow H_2O_2 \quad (3)$$

$$H_2O_2 + O_2^{\bullet -} \rightarrow \bullet OH + OH^- + O_2 \quad (4)$$

$$H_2O_2 + e^- \rightarrow \bullet OH + OH^- \quad (5)$$

$$h^+ + OH^- \rightarrow \bullet OH \quad (6)$$

$$h^+ + H_2O \rightarrow H^+ + \bullet OH \quad (7)$$

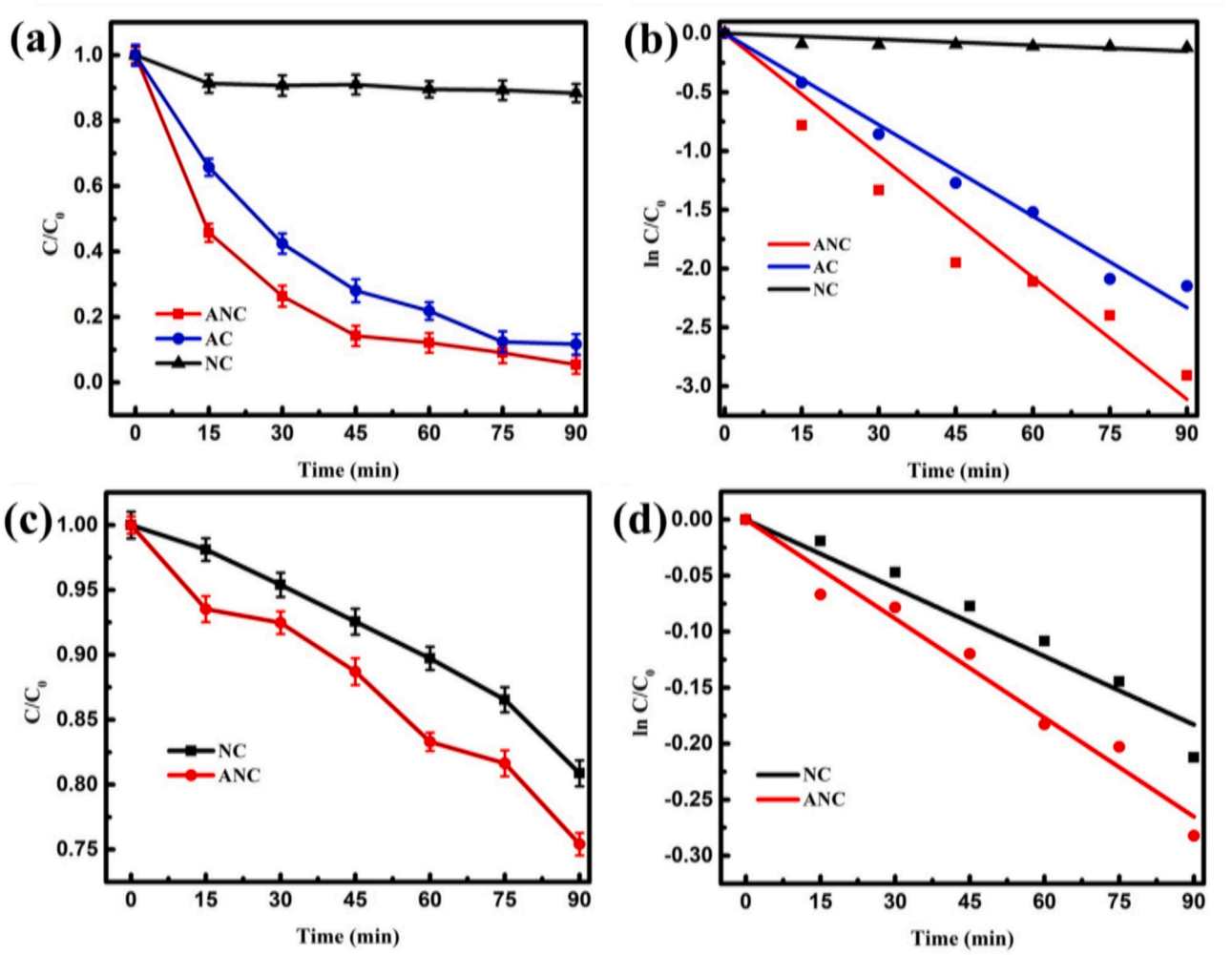

Fig. 7. (a) Degradation pattern (C/C_o vs. time) of MB (0 to 90 min) using NC, AC and ANC photocatalyst, (b) corresponding ln C/C_o against time plot, (c) Degradation profile (C/C_o vs. time) of RhB upon visible light exposure (0 to 90 min) using NC and ANC photocatalyst, and (d) corresponding ln C/C_o vs. time graph.

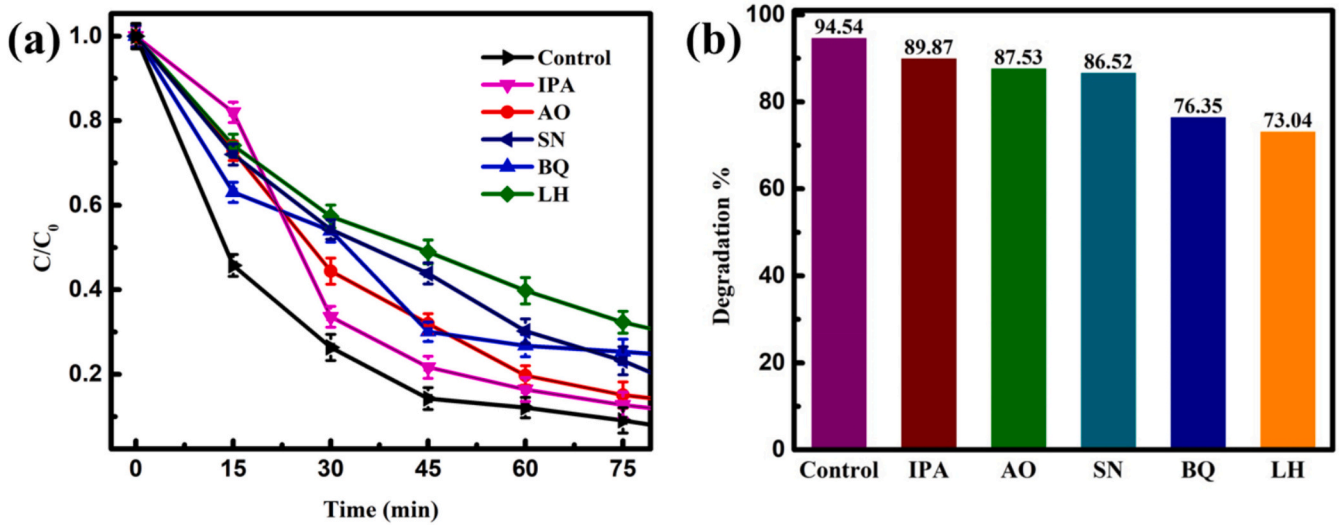

Fig. 8. (a) MB degradation over time and (b) degradation efficiency (%), achieved by the ACT photocatalyst in the presence of different scavenging agents.

$$2 \bullet OH \rightarrow H_2O_2 \quad (8)$$

$$h^+ + O_2^{\bullet -} \rightarrow {}^1O_2 \quad (9)$$

3.7. Photocatalytic mechanism

The photocatalytic mechanism of the ANC photocatalyst, illustrated in Fig. 9, is proposed based on data obtained from UV–Visible spectroscopy, UV-DRS, Tauc plots, active radical quenching experiments, and band edge positions derived from the Mott-Schottky plot. The ANC composite consists of NiO and Ag_2CrO_4, as determined by XRD and XPS spectral analysis. Consequently, the ANC composite features a heterojunction system formed between NiO and Ag_2CrO_4. Furthermore, band gap calculations based on Tauc plots reveal values of 1.77 eV for AC and 3.14 eV for ANC, where the 1.77 eV band gap corresponds to Ag_2CrO_4 and the 3.14 eV band gap to NiO. The valence band maximum (VBM) of NiO, determined from the Mott-Schottky plot, was found to be around 2.02 eV (E vs. NHE, shown in Fig. S17). Similarly, the conduction band minimum (CBM) of AC (Ag_2CrO_4) and ANC was calculated as approximately 0.46 eV and 0.47 eV, respectively. The nearly identical CBM values for AC and ANC indicate that the band extremum positions of Ag_2CrO_4 in ANC remain unchanged. Consequently, the band edge positions of Ag_2CrO_4 in ANC are considered to be 0.47 eV (CBM) and 2.24 eV (VBM), resulting in an overall band gap of 1.77 eV. The band extremum positions of NiO before heterojunction are estimated to be −1.12 eV (CBM) and 2.02 eV (VBM), corresponding to 3.14 eV energy gap. This suggests the apparent formation of a p-n heterojunction between NiO and Ag_2CrO_4. Furthermore, the VBM of ANC was found to be 1.26 eV from the VB XPS spectrum, which is equivalent to 1.32 eV vs NHE using the formula [56]: $E_{NHE} = \phi + E_{VB\ (XPS)} - 4.44\ eV$, where E_{NHE} refers to the potential of standard hydrogen electrode, ϕ represents the work function associated with the XPS spectrometer (4.5 eV for this instrument), and $E_{VB(XPS)}$ is the VBM in eV, obtained from VB XPS spectrum. This can be interpreted as the energy corresponding to the outermost valence electron in the ANC photocatalyst and resulting due to the band bending effect, positioned 0.7 eV above the VBM of NiO (2.02 eV) after heterojunction [57]. The determined band edge alignments before and after heterojunction are shown in Fig. 9(a-b). With the incorporation of Ag nanoparticles (with the Fermi energy at 0.3 eV), a Schottky junction can be effectively formed with NiO, exhibiting rectifying behavior due to the higher Fermi level of Ag relative to p-type NiO [58]. In contrast, Ag forms an Ohmic contact with AC, as its Fermi level is more negative (in potential vs NHE) than that of n-type AC, illustrated in Fig. 9. The photocatalytic mechanism can be understood as follows:

When visible light with an energy of 1.77 eV or higher is incident on the photocatalyst, electrons in Ag_2CrO_4 are excited across the bandgap from the valence band (VB) to the conduction band (CB). These excited electrons subsequently relax to the VB of NiO. Furthermore, upon exposure to visible light with an energy of 2.7 eV or higher, Ag nanoparticles host localized surface plasmon resonance (LSPR), generating highly energetic electrons, as confirmed by plasmonic absorption spectra [22]. Subsequently, through PIRET mechanism, facilitated by dipolar interactions between Ag nanoparticles and NiO, electrons in the VB of NiO gain sufficient energy to transition to the CB of NiO. The occurrence of PIRET in ANC is supported by the overlapping of LSPR band spectra of Ag with the band gap absorption of NiO at around 400 nm (3.1 eV). Through nonradiative relaxation of localized surface plasmon dipoles, resonant energy transfer (RET) can effectively generate electron–hole pairs within the semiconductor. Unlike direct optical excitation, RET drives the generation of photo-induced carriers at energies within and outside the band gap region by transferring energy into near the band edge states that are typically not optically active [59,60]. Furthermore, the Schottky barrier developed at the Ag-NiO interface ensures unidirectional electron transfer into NiO, either through RET or direct electron injection, thereby facilitating their availability for chemical reactions. The occurrence of RET is further supported by the results of active radical quenching experiments, where $^1O_2$, $\bullet O_2^-$ and e^- significantly influence the photocatalytic process in the order $^1O_2 > \bullet O_2^- > e^-$. The electron engagement in the photocatalytic process is likely negligible, as those excited to the CB of NiO are capable of transferring to the CB of Ag_2CrO_4, whose energy level is inadequate to facilitate the reduction of O_2 to $\bullet O_2^-$. However, resonance energy transfer (RET) enables the persistent regeneration of electron-hole pairs in NiO, even after electrons from the CB of Ag_2CrO_4 relax to the VB of NiO. Such an interaction underpins the *Z*-scheme charge migration pathway activated by visible light exposure. In the subsequent step, conduction band electrons of NiO engage in the reduction of oxygen, forming $\bullet O_2^-$ radicals that are essential in MB dye degradation. Moreover, when $\bullet O_2^-$ species interact with the energetic holes residing at the VB of Ag_2CrO_4, they produce $^1O_2$, which further enhances the molecular disintegration of MB. Besides, the photocatalyst can also produce other reactive oxygen species (ROS), such as H_2O_2 and $\bullet OH$, in the presence of atmospheric oxygen within the reactor system [17,55]. These active ROS target the dye molecules breaking them into simpler compounds. The end products, formed through a series of reactions between the charged species and intermediates generated from the initial decomposition of dye molecules, are CO_2 and H_2O [1]. It may be highlighted that the photoexcited holes after relaxing itself from the VB of Ag_2CrO_4

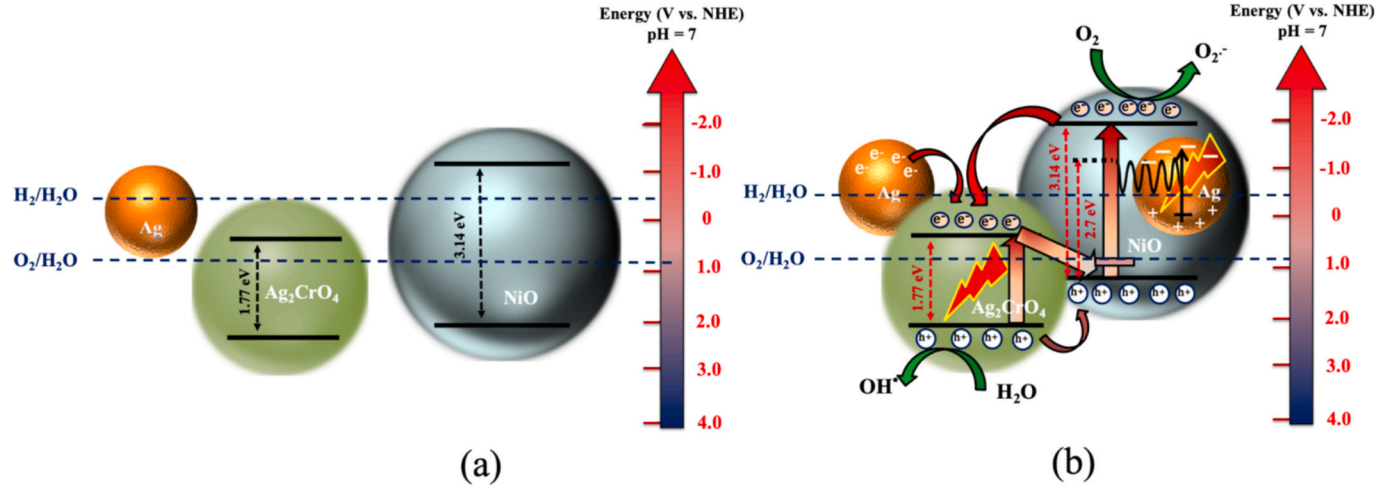

Fig. 9. Proposed photocatalytic mechanism of ANC photocatalyst (a) before, and (b) after heterojunction. A p-n heterojunction with Z-scheme charge transfer dynamics, facilitated by plasmonic Ag via the PIRET mechanism.

to the VB of NiO (VBM = 2.02 eV) lack the necessary potential to generate •OH radicals from water molecules, as this reaction requires an energy of at least 2.3 eV [54]. This finding is further supported by active radical trapping studies, where the suppression of •OH radicals had the least significant impact on photocatalysis. However, since Ag_2CrO_4 alone can facilitate photocatalytic degradation, shown in Fig. 7(a), the energetic holes situated at the VB of Ag_2CrO_4 must play a crucial role in generating •OH radicals, as its VBM lies at around 2.24 eV. This is particularly significant, as the conduction band edge of Ag_2CrO_4 is energetically not favorable for the reduction of O_2 to $\bullet O_2^-$.

Furthermore, the charge transfer behavior of NC, AC and ANC are compared using time-resolved photoluminescence spectra (TRPL) measurements as shown in Fig. 10. The TRPL decay profiles of NC and AC were well described by a single-exponential function, yielding one characteristic lifetime (τ), whereas three different time constants (τ) were found for ANC, indicative of multiple recombination and interfacial relaxation pathways. The corresponding values of the time constants are given in the inset of Fig. 10, along with the average lifetime value calculated for ANC. The average exciton lifetimes for NC and AC are 0.83 ns and 0.82 ns, respectively, whereas ANC exhibits a significantly longer value of 1.43 ns. In addition, the PL transient of ANC exhibits a temporal delay, with the emission maximum appearing at 7.98 ns compared to 6.5 ns for NC and AC. The extended average lifetime and delayed PL response support enhanced charge separation across the heterointerface, consistent with the establishment of a *Z*-scheme heterojunction in ANC. Upon initial photoexcitation of the ANC composite, comprising NiO and Ag_2CrO_4, the photogenerated charge carriers migrate efficiently across the heterointerface, thereby suppressing their rapid recombination. Furthermore, the excited electrons in the CB of Ag_2CrO_4 can undergo nonradiative relaxation to the VB of NiO, rather than radiative recombination. This interfacial charge transfer pathway accounts for the observed emission delay of 1.48 ns in ANC compared to that of the individual NC or AC systems. Following this process, band-to-band recombination of charge carriers takes place in both semiconductor components of ANC, but predominantly in Ag_2CrO_4 considering higher electron population accumulated in its CB after electron migration from the CB of NiO. This direct recombination is therefore associated with the shortest lifetime component (τ_1) of ANC. In addition, trap-assisted interfacial recombination can occur, wherein electrons in the CB of Ag_2CrO_4 recombine with holes in the VB of NiO as a result of *Z*-scheme alignment of band edges. This process corresponds to the intermediate lifetime (τ_2), which is longer than τ_1. Finally, the spatially separated electrons remaining in the CB of NiO and holes localized in the VB of Ag_2CrO_4 through the Z-scheme pathway, would undergo the slowest recombination, giving rise to the longest-lifetime (τ_3). Collectively, these multicomponent decay dynamics in the TRPL spectra strongly support the proposed Z-scheme charge transfer mechanism in ANC. Additionally, EIS study was performed to obtain the Nyquist plots as shown in Fig. S18. Nyquist analysis reveals that the ANC composite exhibits a markedly lower charge-transfer resistance than the NiO counterpart.

4. Conclusion

In this study, Ni—Cr LDH serves as an effective precursor, for the development of Ag/NiO/Ag_2CrO_4 photocatalyst through the strategic incorporation of plasmonic Ag metal. Intriguingly, thermal treatment of the LDH induces its conversion into NiO metal oxide while preserving traces of its initial hydroxide structure, $Ni(OH)_2$, thereby sustaining a complex composition poised for improved catalytic performance. The presence of metal oxide profoundly amplifies crystallinity within the structure, while Ag_2CrO_4 distinctly elevates the photocatalytic ability of the composite photocatalyst Ag@NiO/Ag_2CrO_4 (ANC). The integration of Ag offers two key benefits: it promotes the formation of Ag_2CrO_4 within the original NC matrix; and introduces Ag in its metallic state, imparting strong LSPR effects that boost electron dynamics. The heterojunction with an efficient Z-scheme charge transfer between Ag_2CrO_4 and NiO due to intermediary role of Ag nanoparticles is one of the unique mechanism with continuous regeneration of charge pairs. Additionally, the in-situ growth of Ag_2CrO_4 within the NC structure make ANC as a superior photocatalyst, retaining the layered architecture of the parent LDH structure while improving crystallinity and band edge alignment. ANC exhibits a rate constant 1.3 times higher than AC, and 34 times higher than NC for the degradation of MB without the aid of sacrificial reagents. In essence, this study unveils that the intricate heterojunction matrix photocatalyst, ANC, exhibits exceptional charge carrier dynamics and synergistic effects, contributing to its highly efficient photocatalytic performance. This combined attributes make the material promising with significant prospects for future advancements in related fields.

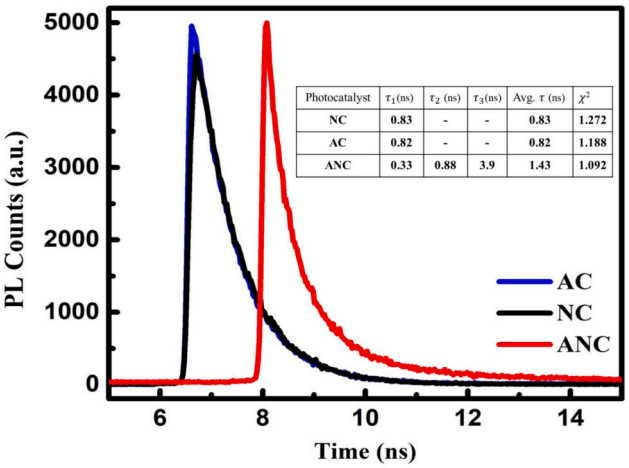

Fig. 10. Time-resolved photoluminescence spectra of NC, AC and ANC.

CRediT authorship contribution statement

Rajmoni Basumatary: Writing – original draft, Visualization, Validation, Methodology, Investigation, Formal analysis, Data curation, Conceptualization. **Phulmani Basumatary:** Methodology, Formal analysis, Data curation. **Saurabh J. Hazarika:** Methodology, Data curation. **Dimpul Konwar:** Writing – review & editing, Methodology, Investigation, Data curation. **Anjalu Ramchiary:** Writing – review & editing, Visualization, Validation, Supervision, Project administration, Methodology, Investigation, Funding acquisition, Formal analysis, Data curation, Conceptualization.

Declaration of competing interest

The authors declare that they have no known competing financial interests or personal relationships that could have appeared to influence the work reported in this paper.

Acknowledgement

We thank Anusandhan National Research Foundation (ANRF-DST), New Delhi, India for providing project fund (Ref. No: EEQ/2023/000212).

Appendix A. Supplementary data

Supplementary data to this article can be found online at https://doi.org/10.1016/j.jwpe.2025.108727.

Data availability

Data will be made available on request.

References

[1] A. Asghar, A.A.A. Raman, W.M.A.W. Daud, Advanced oxidation processes for in-situ production of hydrogen peroxide/hydroxyl radical for textile wastewater treatment: a review, J. Clean. Prod. 87 (2015) 826–838, https://doi.org/10.1016/j.jclepro.2014.09.010.

[2] S. Rehman, R. Ullah, A. Butt, N.D. Gohar, Strategies of making TiO_2 and ZnO visible light active, J. Hazard. Mater. 170 (2009) 560–569, https://doi.org/10.1016/j.jhazmat.2009.05.064.

[3] M. Assis, C.C. de Foggi, V. Teodoro, J.P.D.C. da Costa, C.E. Silva, T. Robeldo, P. F. Caperuccia, C.E. Verganid, R.C. Borrac, I. Sorribese, A.F. Gouveiab, M.A. San-Miguelb, J. Andrés, E. Longo, Surface-dependent photocatalytic and biological activities of Ag_2CrO_4: integration of experiment and simulation, Appl. Surf. Sci. 545 (2021) 148964, https://doi.org/10.1016/j.apsusc.2021.148964.

[4] J.C. Souza, S.C. Lemos, M. Assis, C.H. Fernandes, L.K. Ribeiro, Y. Núñez-de la Rosa, M.D. Teodoro, L. Gracia, J. Andrés, L.H. Mascaro, E. Longo, Boosted photocatalytic activities of Ag_2CrO_4 through Eu^{3+}-doping process, ACS Omega 9 (2024) 35537–35547, https://doi.org/10.1021/acsomega.4c02683.

[5] G.S. Silva, L. Gracia, M.T. Fabbro, L.P. Serejo dos Santos, H. Beltran-Mir, E. Cordoncillo, E. Longo, J. Andres, Theoretical and experimental insight on Ag_2CrO_4 microcrystals: synthesis, characterization, and photoluminescence properties, Inorg. Chem. 55 (2016) 8961–8970, https://doi.org/10.1021/acs.inorgchem.6b01452.

[6] F. Yousefi, M. Haghighi, M. Shabani, Potato-on-rod like of Z-scheme plasmon Ag_2CrO_4-$Ag_2Mo_2O_7$ heterojunction nanophotocatalyst with high stability and accelerated photo-degradation evolution of organic contaminants, Environ. Res. 236 (2023) 116853, https://doi.org/10.1016/j.envres.2023.116853.

[7] Y. Du, J. Li, X. Ma, Q. Guo, Visible light driven mesoporous ag/Ag_2CrO_4/g-C_3N_4 degrades multiple organic pollutants efficiently: synthesis, mechanism, and degradation pathway, Vacuum 226 (2024) 113323, https://doi.org/10.1016/j.vacuum.2024.113323.

[8] N. Gorouhi, M. Haghighi, M. Shabani, C.A. Jaf, Double Z-scheme Ag_2CrO_4/Bi_2O_3–KBi_6O_9Br nanophotocatalysts designed via microwave-assisted combustion-precipitation method for degrading toxic organic dyes, J. Clean. Prod. 450 (2024) 141850, https://doi.org/10.1016/j.jclepro.2024.141850.

[9] B.H. Graimed, Z.H. Jabbar, A.A. Al-Khayfawee, S.H. Ammar, H. Taofeeq, M. Al-Yasiri, The latest trends in NiAl-LDH-based heterojunctions and their photocatalytic capacity for hydrogen evolution under solar light irradiation: photoreaction mechanism justified by DFT calculations, Int. J. Hydrogen Energy 87 (2024) 939–965, https://doi.org/10.1016/j.ijhydene.2024.09.096.

[10] Q. Wang, D. O'Hare, Recent advances in the synthesis and application of layered double hydroxide (LDH) nanosheets, Chem. Rev. 112 (2012) 4124–4155, https://doi.org/10.1021/cr200434v.

[11] H. Boumeriame, E.S. Da Silva, A.S. Cherevan, T. Chafik, J.L. Faria, D. Eder, Layered double hydroxide (LDH)-based materials: a mini-review on strategies to improve the performance for photocatalytic water splitting, J. Energy Chem. 64 (2022) 406–431, https://doi.org/10.1016/j.jechem.2021.04.050.

[12] Z.M. Mir, A. Bastos, D. Höche, M.L. Zheludkevich, Recent advances on the application of layered double hydroxides in concrete—a review, Materials 13 (2020) 1426, https://doi.org/10.3390/ma13061426.

[13] W. Ye, X. Fang, X. Chen, D. Yan, A three-dimensional nickel–chromium layered double hydroxide micro/nanosheet array as an efficient and stable bifunctional electrocatalyst for overall water splitting, Nanoscale 10 (2018) 19484–19491, https://doi.org/10.1039/C8NR05974H.

[14] N.M. Hosny, Synthesis, characterization and optical band gap of NiO nanoparticles derived from anthranilic acid precursors via a thermal decomposition route, Polyhedron 30 (2011) 470–476, https://doi.org/10.1016/j.poly.2010.11.020.

[15] C. Yue, C. Zhu, W. Zheng, J. Qiu, Z. Du, C. Ling, F.Q. Liu, Plasmonic Bi NP-accelerated interfacial charge transfer for enhanced solar-driven ciprofloxacin mineralization, Environ. Sci. Nano 9 (2022) 349–360, https://doi.org/10.1039/D1EN00896J.

[16] C. Ling, C. Yue, R. Yuan, J. Qiu, F.Q. Liu, J.J. Zhu, Enhanced removal of sulfamethoxazole by a novel composite of TiO_2 nanocrystals in situ wrapped-Bi_2O_4 microrods under simulated solar irradiation, Chem. Eng. J. 384 (2020) 123278, https://doi.org/10.1016/j.cej.2019.123278.

[17] C. Yu, H. He, W. Zhou, Z. Liu, L. Wei, Novel rugby-ball-like $Zn_3(PO_4)_2$@C_3N_4 photocatalyst with highly enhanced visible-light photocatalytic performance, Sep. Purif. Technol. 217 (2019) 137–146, https://doi.org/10.1016/j.seppur.2019.02.022.

[18] P. Saikia, C. Gogoi, P.J. Kalita, R.L. Goswamee, Catalytic conversion of high-GWP gases N_2O and CH_4 to syngas (H_2 + CO) on SiO_2@ Ni-Cr layered nano-oxide-coated monolithic catalyst, Environ. Sci. Pollut. Res. 27 (2020) 24939–24953, https://doi.org/10.1007/s11356-020-08589-4.

[19] Y. Qu, W. Zhou, X. Miao, Y. Li, L. Jiang, K. Pan, G. Tian, Z. Ren, G. Wang, H. Fu, A new layered photocathode with porous NiO nanosheets: an effective candidate for p-type dye-sensitized solar cells, Chem. Asian J. 8 (2013) 3085–3090, https://doi.org/10.1002/asia.201300707.

[20] M. Pirhashemi, A. Habibi-Yangjeh, Novel ZnO/Ag_2CrO_4 nanocomposites with n–n heterojunctions as excellent photocatalysts for degradation of different pollutants under visible light, J. Mater. Sci. Mater. Electron. 27 (2016) 4098–4108, https://doi.org/10.1007/s10854-015-4269-4.

[21] R. Basumatary, D. Konwar, B. Basumatary, A. Ramchiary, Plasmonic enhancedbranched Ag sensitized Cu_2O-CuO/TiO_2 heterojunction with unprecedented photocatalytic degradation under visible light, J. Phys. Chem. Solids 180 (2023) 111435, https://doi.org/10.1016/j.jpcs.2023.111435.

[22] Z. Han, L. Ren, Z. Cui, C. Chen, H. Pan, J. Chen, Ag/ZnO flower heterostructures as a visible-light driven photocatalyst via surface plasmon resonance, Appl. Catal. Environ. 126 (2012) 298–305, https://doi.org/10.1016/j.apcatb.2012.07.002.

[23] P. Makuła, M. Pacia, W. Macyk, How to correctly determine the band gap energy of modified semiconductor photocatalysts based on UV–Vis spectra, J. Phys. Chem. Lett. 9 (2018) 6814–6817, https://doi.org/10.1021/acs.jpclett.8b02892.

[24] I. Chanu, P. Krishnamurthi, P.T. Manoharan, Effect of silver on plasmonic, photocatalytic, and cytotoxicity of gold in AuAgZnO nanocomposites, J. Phys. Chem. C 121 (2017) 9077–9088, https://doi.org/10.1021/acs.jpcc.7b02232.

[25] Z. Wang, S.K. Saxena, P. Lazor, H.S.C. O'Neill, An in situ Raman spectroscopic study of pressure induced dissociation of spinel $NiCr_2O_4$, J. Phys. Chem. Solids 64 (2003) 425–431, https://doi.org/10.1016/S0022-3697(02)00328-1.

[26] V. D'Ippolito, G.B. Andreozzi, D. Bersani, P.P. Lottici, Raman fingerprint of chromate, aluminate and ferrite spinels, J. Raman Spectrosc. 46 (2015) 1255–1264, https://doi.org/10.1002/jrs.4764.

[27] M. Hallassi, R. Benrabaa, N.F. Cherif, D. Lerari, R. Chebout, K. Bachari, A. Rubbens, P. Roussel, R.-N. Vannier, M. Trentesaux, A. Löfberg, Characterization and syngas production at low temperature via dry reforming of methane over Ni-M (M= Fe, Cr) catalysts tailored from LDH structure, Catalysts 12 (2022) 1507, https://doi.org/10.3390/catal12121507.

[28] M.T. Fabbro, L. Gracia, G.S. Silva, L.P. Santos, J. Andres, E. Cordoncillo, E. Longo, Understanding the formation and growth of Ag nanoparticles on silver chromate induced by electron irradiation in electron microscope: a combined experimental and theoretical study, J. Solid State Chem. 239 (2016) 220–227, https://doi.org/10.1016/j.jssc.2016.03.050.

[29] O. Dvoynenko, S.L. Lo, Y.J. Chen, G.W. Chen, H.M. Tsai, Y.L. Wang, J.K. Wang, Speciation analysis of Cr (VI) and Cr (III) in water with surface-enhanced Raman spectroscopy, ACS omega. 6 (2021) 2052–2059, https://doi.org/10.1021/acsomega.0c05020.

[30] W. Li, J. Chen, R. Guo, J. Wu, X. Zhou, J. Luo, Facile synthesis of MoS_2/Ag_2CrO_4 composites with improved visible light driven photocatalytic performance, J. Mater. Sci. Mater. Electron. 28 (2017) 14069–14078, https://doi.org/10.1007/s10854-017-7258-y.

[31] J. Al Boukhari, A. Khalaf, R. Sayed Hassan, R. Awad, Structural, optical and magnetic properties of pure and rare earth-doped NiO nanoparticles, Appl. Phys. A Mater. Sci. Process. 126 (2020) 323, https://doi.org/10.1007/s00339-020-03508-3.

[32] K.V. Chandekar, M. Shkir, A. Khan, M.A. Sayed, N. Alotaibi, T. Alshahrani, H. Algarni, S. AlFaify, Significant and systematic impact of yttrium doping on physical properties of nickel oxide nanoparticles for optoelectronics applications, J. Mater. Res. Technol. 15 (2021) 2584–2600, https://doi.org/10.1016/j.jmrt.2021.09.072.

[33] Z. Zhang, H. Huo, L. Wang, S. Lou, L. Xiang, B. Xie, Q. Wang, C. Du, J. Wang, G. Yin, Stacking fault disorder induced by Mn doping in $Ni(OH)_2$ for supercapacitor electrodes, Chem. Eng. J. 412 (2021) 128617, https://doi.org/10.1016/j.cej.2021.128617.

[34] H. Chen, X. Chang, D. Chen, J. Liu, P. Liu, Y. Xue, S. Han, Graphene-karst cave flower-like Ni–Mn layered double oxides nanoarrays with energy storage electrode, Electrochim. Acta 220 (2016) 36–46, https://doi.org/10.1016/j.electacta.2016.10.019.

[35] D. Zhu, C. Guo, J. Liu, L. Wang, Y. Du, S.Z. Qiao, Two-dimensional metal–organic frameworks with high oxidation states for efficient electrocatalytic urea oxidation, Chem. Commun. 53 (2017) 10906–10909, https://doi.org/10.1039/C7CC06378D.

[36] H.Q. Wang, X.P. Fan, X.H. Zhang, Y.G. Huang, Q. Wu, Q.C. Pan, Q.Y. Li, In situ growth of NiO nanoparticles on carbon paper as a cathode for rechargeable Li–O_2 batteries, RSC Adv. 7 (2017) 23328–23333, https://doi.org/10.1039/C7RA02932B.

[37] D.R. Baer, M.H. Engelhard, XPS analysis of nanostructured materials and biological surfaces, J. Electron Spectrosc. Relat. Phenom. 178 (2010) 415–432, https://doi.org/10.1016/j.elspec.2009.09.003.

[38] N. Shevchenko, V. Zaitsev, A. Walcarius, Bifunctionalized mesoporous silicas for Cr (VI) reduction and concomitant Cr (III) immobilization, Environ. Sci. Technol. 42 (2008) 6922–6928, https://doi.org/10.1021/es800677b.

[39] X.Q. Li, J. Cao, W.X. Zhang, Stoichiometry of Cr (VI) immobilization using nanoscale zerovalent iron (nZVI): a study with high-resolution X-ray photoelectron spectroscopy (HR-XPS), Ind. Eng. Chem. Res. 47 (2008) 2131–2139, https://doi.org/10.1021/ie061655x.

[40] J. Luo, X. Zhou, X. Ning, L. Zhan, L. Ma, X. Xu, Z. Huang, J. Liang, Synthesis and characterization of Z-scheme In_2S_3/Ag_2CrO_4 composites with an enhanced visible-light photocatalytic performance, New J. Chem. 41 (2017) 845–856, https://doi.org/10.1039/C6NJ02934E.

[41] Y. Deng, L. Tang, G. Zeng, J. Wang, Y. Zhou, J. Wang, J. Tang, Y. Liu, B. Peng, F. Chen, Facile fabrication of a direct Z-scheme Ag_2CrO_4/g-C_3N_4 photocatalyst with enhanced visible light photocatalytic activity, J. Mol. Catal. A Chem. 421 (2016) 209–221, https://doi.org/10.1016/j.molcata.2016.05.024.

[42] H. Yang, H. Hao, Y. Zhao, Y. Hu, J. Min, G. Zhang, J. Bi, S. Yan, H. Hou, An efficient construction method of S-scheme Ag_2CrO_4/$ZnFe_2O_4$ nanofibers heterojunction toward enhanced photocatalytic and antibacterial activity, Colloids Surf. A Physicochem. Eng. Asp. 641 (2022) 128603, https://doi.org/10.1016/j.colsurfa.2022.128603.

[43] B. Ali, E. Abdelkader, B. Naceur, C. Houcine, L. Nadjia, B. Nourredine, Sunlight-driven photocatalytic degradation of Rhodamine B by BiOCl and TiO_2 deposited on NiCr-LDH, Int. J. Environ. Anal. Chem. 103 (2023) 6722–6741, https://doi.org/10.1080/03067319.2021.1959570.

[44] K. Atacan, N. Güy, B. Boutra, M. Özacar, Enhancement of photoelectrochemical hydrogen production by using a novel ternary Ag_2CrO_4/GO/$MnFe_2O_4$ photocatalyst, Int. J. Hydrogen Energy 45 (2020) 17453–17467, https://doi.org/10.1016/j.ijhydene.2020.04.268.

[45] S.K. Pandey, M.K. Tripathi, V. Ramanathan, P.K. Mishra, D. Tiwary, Highly facile Ag/NiO nanocomposite synthesized by sol-gel method for mineralization of rhodamine B, J. Phys. Chem. Solids 159 (2021) 110287, https://doi.org/10.1016/j.jpcs.2021.110287.

[46] Y. Gan, Y. Wei, J. Xiong, G. Cheng, Impact of post-processing modes of precursor on adsorption and photocatalytic capability of mesoporous TiO_2 nanocrystallite aggregates towards ciprofloxacin removal, Chem. Eng. J. 349 (2018) 1–16, https://doi.org/10.1016/j.cej.2018.05.051.

[47] M. Zhang, J. Xiong, H. Yang, Z. Wen, R. Chen, G. Cheng, Surface potential/wettability and interface charge transfer engineering of copper-oxide (Cu–MO_x, M = W, Ti, and Ce) hybrids for efficient wastewater treatment through adsorption–photocatalysis synergy, Ind. Eng. Chem. Res. 59 (2020) 15454–15463, https://doi.org/10.1021/acs.iecr.0c02663.

[48] G. Cheng, M. Jiang, W. Zhang, Z. Wen, J. Xiong, Uncovering fabrication approach impact on photocatalytic ciprofloxacin (CIP) antibiotic degradation of brookite TiO_2, Sustain. Mater. Technol. 41 (2024) e01018, https://doi.org/10.1016/j.susmat.2024.e01018.

[49] M.W. Alam, A. BaQais, T.A. Mir, I. Nahvi, N. Zaidi, A. Yasin, Effect of Mo doping in NiO nanoparticles for structural modification and its efficiency for antioxidant, antibacterial applications, Sci. Rep. 13 (2023) 1328, https://doi.org/10.1038/s41598-023-28356-y.

[50] M.S. NourEldien, M.Y. Nassar, I.M. Ibrahim, H.M. Aly, Tandem NiO-Ni $(OH)_2$/VS_2 Nanosheets: a robust photocatalyst for hydrogen evolution, Mater. Adv. 5 (2024) 9107, https://doi.org/10.1039/D4MA00789A.

[51] D. Dodoo-Arhin, F.P. Buabeng, J.M. Mwabora, P.N. Amaniampong, H. Agbe, E. Nyankson, D.O. Obada, N.Y. Asiedu, The effect of titanium dioxide synthesis technique and its photocatalytic degradation of organic dye pollutants, Heliyon 4 (2018) e00681, https://doi.org/10.1016/j.heliyon.2018.e00681.

[52] Z. He, C. Sun, S. Yang, Y. Ding, H. He, Z. Wang, Photocatalytic degradation of rhodamine B by Bi_2WO_6 with electron accepting agent under microwave irradiation: mechanism and pathway, J. Hazard. Mater. 162 (2009) 1477–1486, https://doi.org/10.1016/j.jhazmat.2008.06.047.

[53] K. Yu, S. Yang, H. He, C. Sun, C. Gu, Y. Ju, Visible light-driven photocatalytic degradation of rhodamine B over $NaBiO_3$: pathways and mechanism, J. Phys. Chem. A 113 (2009) 10024–10032, https://doi.org/10.1021/jp905173e.

[54] J. Li, M. Jiang, H. Zhou, P. Jin, K.M. Cheung, P.K. Chu, K.W. Yeung, Vanadium dioxide nanocoating induces tumor cell death through mitochondrial electron transport chain interruption, Glob. Chall. 3 (2019) 1800058, https://doi.org/10.1002/gch2.201800058.

[55] M. Cho, H. Chung, W. Choi, J. Yoon, Linear correlation between inactivation of E. coli and OH radical concentration in TiO_2 photocatalytic disinfection, Water Res. 38 (2004) 1069–1077, https://doi.org/10.1016/j.watres.2003.10.029.

[56] X. Pan, Y. Meng, Q. Liu, M. Xu, Construction of Ag_3PO_4/g-C_3N_4 Z-scheme heterojunction composites with visible light response for enhanced photocatalytic degradation, Molecules 29 (2024) 3774, https://doi.org/10.3390/molecules29163774.

[57] S. Pahi, B. Mahapatra, A. Behera, S.K. Singh, R.K. Patel, Fermi level induced band edge alignment and band bending in Ag_3PO_4/Cu_2O pn heterojunction for proficient photocatalytic applications, Mater. Chem. Phys. 305 (2023) 127992, https://doi.org/10.1016/j.matchemphys.2023.127992.

[58] A. Gangan, A. Fahmy, S.A. Shaban, Z.M. El-Bahy, Plasma modification of the structural, morphological, and catalytic activity of Fe_3O_4@SiO_2@TiO_2 core–shell system, Adv. Compos. Hybrid Mater. 8 (2025) 1–20, https://doi.org/10.1007/s42114-025-01260-x.

[59] S.K. Cushing, J. Li, F. Meng, T.R. Senty, S. Suri, M. Zhi, M. Li, A.D. Bristow, N. Wu, Photocatalytic activity enhanced by plasmonic resonant energy transfer from metal to semiconductor, J. Am. Chem. Soc. 134 (2012) 15033–15041, https://doi.org/10.1021/ja305603t.

[60] J. Li, S.K. Cushing, F. Meng, T.R. Senty, A.D. Bristow, N. Wu, Plasmon-induced resonance energy transfer for solar energy conversion, Nat. Photonics 9 (2015) 601–607, https://doi.org/10.1038/nphoton.2015.142.

Journal of Physics and Chemistry of Solids 180 (2023) 111435

Contents lists available at ScienceDirect

Journal of Physics and Chemistry of Solids

journal homepage: www.elsevier.com/locate/jpcs

Plasmonic enhanced branched Ag sensitized Cu_2O–CuO/TiO_2 heterojunction with unprecedented photocatalytic degradation under visible light

Rajmoni Basumatary [a], Dimpul Konwar [b], Bablu Basumatary [c], Anjalu Ramchiary [a,*]

[a] Nano Energy Materials Laboratory, Department of Physics, Bodoland University, Rangalikhata, Kokrajhar, Assam, 783370, India
[b] Department of Materials Science and Engineering, Gachon University, Bokjung-dong, Seongnam-si, Gyeonggi-do, 1342, Republic of Korea
[c] Physical Sciences Division, Institute of Advanced Study in Science and Technology, Guwahati, Assam, 781035, India

ARTICLE INFO

Keywords:
Photocatalysis
Heterojunction
Localized Surface Plasmon Resonance
Dye degradation
Visible light active

ABSTRACT

A novel plasmonic Ag assisted Cu_2O–CuO/TiO_2 heterojunction photocatalyst was prepared using a facile sol-gel technique, and its MB degradation efficiency was explored. The physicochemical, morphostructural, and spectroscopic analyses using XRD, UV–vis-DRS, SEM, TEM, Raman, ESR, PL and XPS showed the formation of Ag@Cu_2O–CuO/TiO_2 hybrid photocatalyst, exhibiting surface plasmon resonance (SPR) and interfacial ternary heterojunctions. The SPR exhibited by the bulbous branched Ag nanostructures resulted in broad visible light absorption that extended into the near-infrared region. This plasmonic-heterojunction hybrid photocatalyst has shown excellent photocatalytic degradation, far surpassing the performance of its pristine counterparts under visible light illumination. The improved photocatalytic degradation of MB is attributable to the synergistic impact of reduced electron-hole pair recombination owing to Cu_2O–CuO/TiO_2 ternary junction, broad visible light absorption and near-field enhancement through the surface plasmon resonance effect. The current study demonstrates an integrated plasmonic-heterojunction photocatalytic system that offers a promising avenue for enhancing photocatalytic performance in dye-contaminated water treatment.

1. Introduction

The rapid industrialization has resulted in the release of a wide range of pollutants into the environment, some of which are toxic [1]. These pollutants have the potential to damage the environment as well as the ecosystem. Synthetic dyes released by textile industries, in particular, are a major source of pollution that is detrimental to both humans and animals [2,3]. Therefore, it is imperative to devise a sustainable mechanism for the removal of these dyes before they are released into the environment. Hitherto, semiconductor-based photocatalysis has attracted the attention of researchers across the world for its ability to eliminate organic contaminants efficiently and sustainably [4]. Many semiconductor and metal/semiconductor composite nanoparticles with the appropriate bandgap and band edge locations exhibits photocatalytic process. Compared to the conventional biological, physical, and chemical methods of removing dyes, the metal/metal oxide-based UV–visible light-driven photocatalysis offers several advantages, including fast oxidation, non-toxic by-products, affordability, and eco-friendliness [3]. However, unmodified semiconductors have several drawbacks, such as high recombination, limited photon absorption, and few active sites for photocatalytic processes. To achieve a photocatalyst with exceptional photocatalytic performance requires controlling essential attributes, including phase composition, morpho-structure, surface chemical state, and optoelectrical properties, through the synthesis method and process conditions [5].

Titanium dioxide (TiO_2) is one of the widely explored semiconductor photocatalysts because of its rapid oxidative reaction, high chemical stability, non-toxicity, and low price [6,7]. However, large bandgap (3.2 eV), fast electron-hole recombination, and low surface area of unmodified TiO_2 results in poor photocatalytic efficiency under visible light [8,9]. Recently, the heterostructures between semiconductor photocatalyst has been intensively investigated due to swift spatial segregation of the light-induced electron-hole pairs at the junction [10–13]. Li et al. demonstrated that multi-heterojunction with type I and type II arrangement that showed more photocatalytic activity than the single heterojunction [14]. Another study reported that the direct

* Corresponding author.
E-mail addresses: onjalu@gmail.com, a.ramchiary_88@yahoo.com (A. Ramchiary).

https://doi.org/10.1016/j.jpcs.2023.111435
Received 29 January 2023; Received in revised form 1 May 2023; Accepted 10 May 2023
Available online 10 May 2023

Z-scheme heterojunction of TiO_2/g-C_3N_4 accelerated the photocatalytic activity due to effective charge separation though the interface [15]. A potential gradient develops at the heterojunction interface due to the energy band mismatch of the semiconductors, facilitating quick separation of photogenerated charge carriers [16,17]. Zhang et al. fabricated a bamboo-like architecture of Ag/CuO/TiO_2 photocatalyst, which integrates p-n heterojunction and Schottky junction, exhibits high photoactivity due to improved light absorption, maximized charge-carrier separation and large active sites [18].

Plasmonic photocatalysts are another type of photocatalyst that have received much interest because of the unique phenomenon of plasmonic resonance, which offers light absorption tunability throughout a wide range of spectral regions [19]. Several studies have been reported on the enhancement in the photocatalytic activity using different shapes and sizes of plasmonic metals with increasing visible light response [20–23]. Depending on the specific shape or structure of a plasmonic metal, the number of plasmonic resonance peaks and their intensity varies. As the metal shape becomes less symmetrical, more resonances peaks are observed. For instance, in shapes with limited symmetry, such as nanobars, polarization can occur in two directions: along the longer axis and the shorter axis. This results in resonant oscillation at two distinct wavelengths of visible light [24,25]. In contrast, an isotropic sphere exhibits resonance at a specific wavelength in the light spectrum, resulting in a single peak in the absorbance spectra. In addition, a particular symmetry in the plasmonic structure facilitates charge carrier separation than others, which produces a strong dipole and a higher plasmonic resonance peak intensity [26]. Silver nanoparticle (AgNPs) are primarily investigated for plasmonic applications due to their several advantages, including a high-quality factor over the near UV–Vis-IR spectrum, and increased electrical and thermal conductivity [27]. The induced localized field due to surface plasmon resonance (LSPR) significantly reduces photoexcited charge carrier recombination and facilitates electron injection from plasmonic metal to host semiconductor [28]. Nagajyothi et al. highlighted the significant features of LSPR, where the plasmonic metal nanoparticles absorb and scatter light in the visible and near-infrared regions, resulting in a generation of strong local electric fields around the nanoparticles [3]. The average photon path length in metal-semiconductor composites increases as a result of the light absorption and re-emission in plasmonic metals, resulting in a higher activation rate of incident photons. Further, in comparison to single-component systems, multicomponent heterojunction systems comprising multiple activated components have been demonstrated to enable efficient spatial separation of photo-induced electron-hole pairs via multistep charge transfer at the interfaces, resulting in enhanced photocatalytic performance [5]. The formation of multiple p-n junctions and the LSPR effect of Ag nanoparticles in M@Cu_xO/ZnO (M = Au, Ag) was demonstrated by Gavade et al. [29]. According to their report, the improved visible light-driven catalytic activity is ascribed to the synergistic effect of the wider spectral band, efficient transfer of photogenerated charge carriers, and strong LSPR impact.

Herein, we have initially synthesized bulbous structured Ag nanoparticles using a facile method and later sensitized on CuO/TiO_2 heterojunction photocatalyst and finally obtained a plasmonic-heterojunction hybrid material (Ag@Cu_2O–CuO/TiO_2) via a post thermal treatment. The Cu_2O–CuO/TiO_2 ternary junction enhanced the charge carrier separation through the interface between the semiconductors. The mismatch in band edge positions between Cu_2O, CuO and TiO_2 produce a built-in field near the junctions that plays a vital role in boosting the photocatalytic degradation. Additionally, the bulbous Ag nanoparticles exhibit broad absorption across the visible range, which further enhances the catalyst's performance in visible light. We have used methylene blue (MB) as a test pollutant for photocatalytic degradation. The photocatalytic activity of Ag@Cu_2O–CuO/TiO_2 was found to be 26.5 times superior to the pure TiO_2 counterpart. A comparative analysis of the photocatalytic activity of recently reported similar photocatalysts is shown in Table S1 in supplementary information (SI). The plasmonic charge carrier injection into the photocatalyst and the ease in the charge transfer between the interface was demonstrated via a ternary interfacial junction.

2. Experimental section

2.1. Reagents used

Titanium isopropoxide [$Ti(OCH(CH_3)_2)_4$] was purchased from Alfa Aesar. Silver nitrate [$AgNO_3$], 2-propanol [$(CH_3)_2CHOH$], Ammonia solution [NH_3], Ascorbic acid [$C_6H_8O_6$], and nitric acid [HNO_3] were supplied by Merck, India. Sodium hydroxide pellets [NaOH] and copper sulphate pentahydrate [$CuSO_4{\cdot}5H_2O$] obtained from Avantor performance materials India limited. Ammonium oxalate [$(NH_4)_2C_2O_4$] was purchased from Rankem, India and *p*-Benzoquinone [$C_6H_4O_2$] form Sigma-Aldrich, and L-histidine [$C_6H_9N_3O_2$] was obtained from Loba Chemie Pvt Ltd.

2.2. Synthesis of Ag@Cu_2O–CuO/TiO_2 photocatalyst and its counterparts

2.2.1. Preparation of pure TiO_2, CuO and bulbous Ag structure

In the synthesis of pure TiO_2, a mixture of $Ti(OCH(CH_3)_2)_4$ and $(CH_3)_2CHOH$ at a particular 1:10 vol ratio was obtained and stirred rapidly. Half an hour later, 200 μL of H_2O was added dropwise at stirring condition. Again after 30 min, 1 mL of 1 M HNO_3 was added to the mixture. This mixture solution was continuously kept under stirring condition for the next 24 h. A semi-gel precipitation was obtained after aging for a few hours. The product was then dried at 80–100 °C, followed by pulverization into a fine powder, and then finally calcined at 600 °C for 2 h.

To obtain the CuO co-catalyst, a simple wet-chemical procedure was adopted that required a moderately low temperature (~80 °C) condition. First, 100 mL solution of 0.0216 M copper sulfate pentahydrate ($CuSO_4{\cdot}5H_2O$) was prepared. Afterward, 500 μL of 14.7 M ammonium solution was added under constant stirring conditions. Next, 25 mL NaOH (0.1 M) solution was mixed to the above suspension followed by 10 mL ascorbic acid (0.1 M) addition and kept at ~80 °C for 50 min under constant stirring. After obtaining a red-brown precipitate, it was washed several times and calcined for 2 h at 600 °C. The product has been found to be in the Cu_2O phase in its raw form (before calcination).

In a typical synthesis of bulbous branched Ag nanostructure, 10 mL L-ascorbic acid (4.6 mM) was blended with 10 mL silver nitrate ($AgNO_3$), and the resultant mixture was centrifuged to obtain the Ag product.

2.2.2. Preparation of CuO/TiO_2 and Ag@Cu_2O–CuO/TiO_2 photocatalyst

In order to synthesize CuO/TiO_2, we have prepared a solution of 2 mL titanium isopropoxide and 20 mL isopropanol. After 30 min of vigorous stirring, 0.1 g of previously prepared CuO dispersed uniformly in 50 mL isopropanol was added. Then, after 50 min, 1 mL of concentrated HNO_3 solution was mixed with the solution. The suspension was stirred for 24 h and kept in the ambient condition for another 24 h. The obtained sample was ground into a fine powder and calcined at 600 °C for 2 h.

In the Ag@Cu_2O–CuO/TiO_2 photocatalyst synthesis, Ti(IV)-isopropoxide and isopropanol were mixed by stirring it constantly and vigorously. After 30 min, 0.0045 g of well-dispersed Ag was added to the solution. Subsequently, 0.20 g of CuO was uniformly dispersed in 50 mL isopropanol, and 1 mL of concentrated HNO_3 was added to the mixture. It was then stirred for 72 h. Finally, the supernatant was discarded, and the obtained product was calcined at 600 °C for 2 h.

2.3. Characterization of photocatalysts

X-ray diffraction was used to analyze the crystalline phases and structural characteristics of the produced powder samples (Bruker-D8-

AXS Adv. X-ray diffractometer, CuKα radiation, scan speed: 0.5 step/second). Scanning electron microscopy (SEM, Hitachi S4200, SIGMA VP FESEM, ZEISS) and transmission electron microscopy (TEM, FEI Tecnai G^2 F20; JEM-100 CX II a; JEM-2100 PLUS (HR), JEOL) were used to examine the morphological aspects of the prepared samples. The optical absorption was investigated using a UV/Visible Scanning Spectrophotometer (Shimadzu UV-1800). Raman activity was investigated using the Renishaw basis series with 514 nm lasers Raman spectrophotometer. The ESR spectra were obtained from an electron spin resonance (ESR) spectrometer model: JES-FA200, JEOL. The photoluminescence spectrophotometer (FluoroMax-4C; 1379D, UK) was employed to record the photoluminescence spectra. The electronic state and chemical compositions of the produced powder samples were studied using X-ray photoelectron spectroscopy equipped with Al K-Alpha X-ray source (Thermo-125 Scientific, UK). An electrochemical workstation (Metrohom-autolab, PGSTATE-302 N) was used to obtain the photoelectrochemical (PEC) measurements of the photocatalyst.

2.4. Photocatalytic experiment

Photocatalytic degradation evaluation of the photocatalysts was performed by degradation of MB using a visible light source (SANSI LED bulb, $\lambda > 400$ nm). The intensity of visible irradiance is 46 W/cm^2 (measured by Metravi light detector). A solution of MB was prepared with 0.01 mM concentration and 0.5 gL^{-1}catalyst loading. Before light irradiation, the equilibrium adsorption-desorption state of the catalyst-loaded MB solution was obtained. Subsequently, the liquid suspension was illuminated with light, and a particular amount was collected at 15-min intervals. The optical density of the degradation were measured using a spectrophotometer (Shimadzu 1900i).

2.5. Free radical quenching test

The photocatalytic degradation of organic pollutants depends on reactive species including holes (h^+), electrons (e^-), superoxide radicals (O_2^-), hydroxyl radicals ($^\bullet OH$), and singlet oxygen ($^1O_2$). The role of active species generated in the photocatalysis process was investigated by using quenching agents ammonium oxalate (AO), silver nitrate (SN), *p*-benzoquinone (BQ), isopropyl alcohol (IPA), and L-histidine (LH) for h^+, e^-, $^\bullet O_2^-$, $^\bullet OH$, and $^1O_2$, respectively [30–32]. The MB concentration, catalyst loading, and evaluation process were the same as in the photocatalytic degradation experiment.

3. Results and discussion

3.1. XRD and UV–vis-DRS analysis

XRD patterns of TiO_2, CuO, CuO/TiO_2 and $Ag@Cu_2O–CuO/TiO_2$ are shown in Fig. 1 (a). The diffraction spectra of pristine TiO_2, CuO/TiO_2 and $Ag@Cu_2O–CuO/TiO_2$ at $2\theta = 27.4^o$, 36.1^o, 41.3^o, 44.1^o, 54.2°, 56.7°, 64.1^o and 69.1^o corresponds to the rutile phase (PDF no: 894920). These peaks represent the planes (110), (101), (111), (210), (211), (220), (310) and (301), respectively. No peaks corresponding to anatase phase were observed in TiO_2 and CuO/TiO_2. However, the observed peaks at $2\theta = 25.3^o$, 48.1^o and 62.7^o in $Ag@Cu_2O–CuO/TiO_2$ are due to the anatase phase of TiO_2, which correspond to the planes (101), (200) and (204) (PDF no: 894921). The presence of the anatase phase in the $Ag@Cu_2O–CuO/TiO_2$ sample could be ascribable to the Ag incorporation which prevents the growth of rutile phase [33]. A similar result was observed in $Ag@TiO_2$ sample shown in Fig. S1 in SI. Notably, the as-prepared CuO (before calcination) has the form of Cu_2O, shown in Fig. S1 in supplementary information (SI), which was transformed to CuO after heat treatment at 600 °C [34]. The major XRD peaks of CuO were located at $2\theta = 35.2^o$, 38.6^o, 48.7^o, 53.4^o, 61.4^o, and 67.9^o (PDF no: 892530). The presence of CuO is confirmed by the appearance of peaks at 35.2^o and 38.6^o in CuO/TiO_2 and $Ag@Cu_2O–CuO/TiO_2$. However, the peaks related to Cu_2O and Ag were not observed in the XRD spectrum of $Ag@Cu_2O–CuO/TiO_2$ which might be due to the low concentration compared to TiO_2. The crystallite size determined by the Debye-Scherrer equation, for CuO is ~11 nm, while the crystallite size of

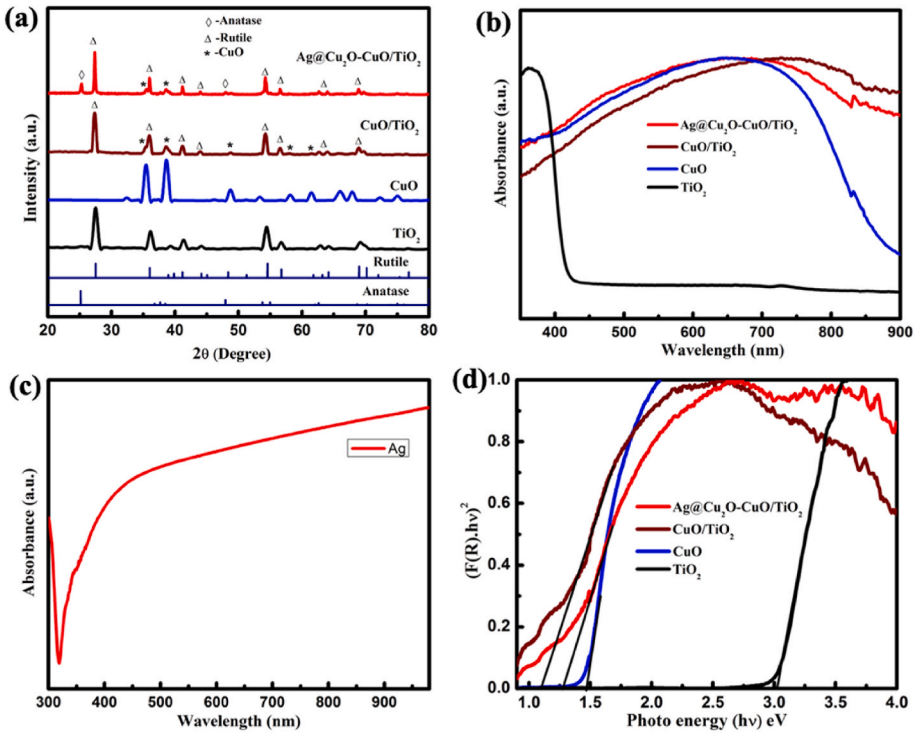

Fig. 1. (a) XRD pattern and (b) UV–Vis-DRS of TiO_2, CuO, CuO/TiO_2 and Ag@ Cu_2O CuO/TiO_2. (c) UV–vis absorbance spectra of bulbous Ag. (d) Bandgap determination of TiO_2, CuO, CuO/TiO_2 and $Ag@Cu_2O–CuO/TiO_2$ using Tauc plot.

TiO_2 is ~17 and ~35 nm, in CuO/TiO_2 and $Ag@Cu_2O–CuO/TiO_2$, respectively.

Fig. 1(b) displays the absorbance spectra of TiO_2, CuO, CuO/TiO_2 and $Ag@Cu_2O–CuO/TiO_2$. Pure TiO_2 shows sharp absorption onset in the UV region at around 387 nm, while CuO/TiO_2 and $Ag@Cu_2O–CuO/TiO_2$ sample exhibits an extended absorption over the visible range of 400–800 nm. The absorbance spectrum of Ag is highly broad that extends into the near-infrared (NIR) region, attributable to the branched nature of silver (illustrated in Fig. 1(c)) [35,36]. The Tauc plot of the Kubelka-Munk function for calculating the optical bandgap is shown in Fig. 1(d) [37]. The obtained bandgaps of the samples are 3.02, 1.47, 1.17 and 1.24 eV for TiO_2, CuO, CuO/TiO_2 and $Ag@Cu_2O–CuO/TiO_2$, respectively. There was no change in the bandgap of TiO_2 and CuO after Ag incorporation. The absorbance spectra and the Tauc plot for determination of the bandgap of $Ag@TiO_2$, Ag@CuO, and Cu_2O are shown in Figs. S2(a–b) in SI.

3.2. Raman, ESR and photoluminescence (PL) analysis

The Raman spectra of TiO_2, CuO/TiO_2, and $Ag@Cu_2O–CuO/TiO_2$ are displayed in Fig. 2(a). The pure TiO_2 revealed the typical stretching peaks of the rutile phase at 140, 447.1, and 607.9 cm^{-1}, which correspond to the symmetric modes B_{1g}, E_g, and A_{1g} [38–40]. Additionally, the broad and mid-intensity signal detected at 238 cm^{-1} is attributable to the two-photon scattering of the rutile phase [40]. The peak observed at 277 (A_g) and 616 cm^{-1} (B_g) in CuO/TiO_2 and $Ag@Cu_2O–CuO/TiO_2$ are related to CuO [41–43]. In $Ag@Cu_2O–CuO/TiO_2$, the Raman signals at 144, 197, 396, and 513 cm^{-1} with symmetries of E_g, E_g, B_{1g}, and (A_{1g} + B_{1g}) represent the anatase phase, whereas the signals at 143, 443, and 608 cm^{-1} with symmetries of B_{1g}, E_g and A_{1g} denote the rutile phase [42]. Furthermore, the Raman spectrum of $Ag@Cu_2O–CuO/TiO_2$ reveals the presence of Cu_2O at 410 (multi-phonon scattering) and 515 cm^{-1} (T_{2g}), which accords with the XPS results [43–45]. The presence of the anatase phase in the $Ag@TiO_2$ counterpart was also observed (shown in Fig. S3 in SI).

The electron spin resonance (ESR) study was performed to understand the presence of oxygen vacancy or Ti^{3+} in the photocatalyst. ESR spectrum of TiO_2, CuO/TiO_2, and $Ag@Cu_2O–CuO/TiO_2$ are displayed in Fig. 2(b). The *g*-value was obtained using the relation $g = h\nu/\beta H_o$, where *h* is the plank constant, ν is the frequency, β is the Bohr magnetron, and H_o is the resonance magnetic field [46]. The ESR resonance peak at g = 1.98 in pure TiO_2 corresponds to the Ti^{3+} species [47]. The observed ESR signals of CuO/TiO_2 and $Ag@Cu_2O–CuO/TiO_2$ at g = 2.13 are attributable to Cu^{2+} [48,49]. The ESR peak intensity at g = 2.13 is decreased considerably after Ag incorporation in $Ag@Cu_2O–CuO/TiO_2$, indicating the presence of Cu_2O [48].

The photoluminescence (PL) measurement provides crucial information about the separation, trapping, and migration of the photoexcited electron holes. Fig. 2(c) shows the room temperature PL spectra of TiO_2, CuO, CuO/TiO_2, and $Ag@Cu_2O–CuO/TiO_2$ at an excitation wavelength of 320 nm. The pristine TiO_2 and CuO/TiO_2 show emission spectra in a wide wavelength range from 400 to 550 nm, which arises due to the self-trapped excitons, oxygen vacancies, and surface state [50]. However, in the case of CuO, no discernible peaks with significant intensity are detectable. It can be observed that the resultant PL emission spectrum of CuO/TiO_2 is significantly quenched compared to TiO_2, which implies the substantial decrease in the recombination of electron-hole pairs. This is because the photogenerated electrons in the conduction band (CB) of TiO_2 migrate to the CB of CuO. The emission peak located at around 419 and 415 nm in TiO_2 and CuO/TiO_2 respectively, is attributed to the band edge emission corresponding to the band gap of TiO_2 [51]. The emission peaks produced at 434 and 466 nm are attributed to the intrinsic structural defects and the surface oxygen vacancies, respectively [50]. Additionally, the peak detected at 443 nm may be originating from the self-trapped excitons in TiO_6 octahedra [52]. Notably, the PL emission of $Ag@Cu_2O–CuO/TiO_2$ was further

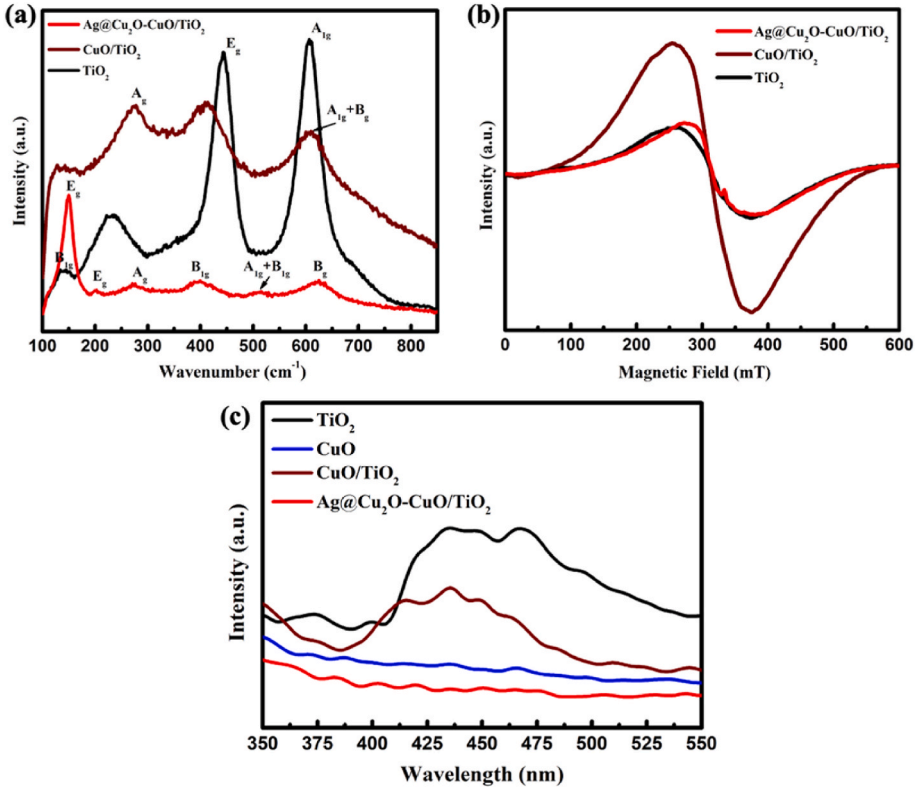

Fig. 2. (a) Raman, (b) Room temperature ESR spectra, of TiO_2, CuO/TiO_2, $Ag@Cu_2O–CuO/TiO_2$, and (c) Photoluminescence spectra of TiO_2, CuO, CuO/TiO_2, and $Ag@Cu_2O–CuO/TiO_2$.

quenched to extremely low intensity, indicating the efficient electron-hole separation and increased lifetime of the carriers. The heterojunction Cu_2O–CuO/TiO_2 and the Schottky junction created with metallic Ag are responsible for facilitating charge separation and transfer through the interfaces.

3.3. XPS analysis

XPS was used to study the chemical and electronic states of the prepared catalysts. Fig. 3(a) depicts the complete scanning spectra of TiO_2, CuO, CuO/TiO_2, and Ag@Cu_2O–CuO/TiO_2, revealing the presence of the key components C, Ti, O, Ag, and Cu. The signal of carbon appearing at binding energy (BE) 284.8 eV is due to the presence of adventitious carbon [53]. The entire survey XPS spectra of the counterparts Ag@TiO_2 and Ag@CuO are also displayed with the key elements Ag, Ti, Cu, O and C, shown in Fig. S4 in SI.

The characteristic Ti 2p XPS spectra of TiO_2, CuO/TiO_2, and Ag@Cu_2O–CuO/TiO_2 are presented in Fig. 3(b), (c), and (d), respectively. The well-resolved Ti spectra of TiO_2 show two distinct peaks at BE 458.5 and 464.1 eV, which correspond to the Ti ($2p_{1/2}$) and Ti ($2p_{3/2}$) doublets, respectively, reveal the existence of the Ti^{4+} oxidation state [54–56]. Similarly, the Ti 2p doublets are observed at BE 458.6 and 464.3 eV for both CuO/TiO_2, and Ag@Cu_2O–CuO/TiO_2. The Ti 2p spectra were deconvoluted into three peaks. For the pristine TiO_2 sample, the deconvoluted peaks are located at 458.5, 460.3, and 464.1 eV (given in Fig. 3(b)). The peak at 460.3 eV represents the Ti^{3+} ($2p_{1/2}$) oxidation state [54,57]. The XPS peaks are found to be shifted to 458.6, 460.6, and 464.3 eV in CuO/TiO_2 and Ag@Cu_2O–CuO/TiO_2. The larger XPS peak fit area owing to the Ti^{3+} ($2p_{1/2}$) state in (Fig. 3(c)) and Ag@Cu_2O–CuO/TiO_2 (Fig. 3(d)) implies the formation of additional oxygen vacancies. Correspondingly, the Ti 2p XPS spectrum of Ag@TiO_2 was also deconvoluted into three peaks at BE 458.6, 460.5, and 464.4 eV, shown in Fig. S5(a) in SI.

The high-resolution O1s XPS measurements of the prepared photocatalysts are presented in Fig. 4. In pristine TiO_2, the peaks at BE 529.5, 530.1, and 531.5 eV are attributable to lattice-oxygen, Ti_2O_3, and surface adsorbed O_2 (Fig. 4 (a)) [54,58,59]. Fig. 4 (b), (c) and (d) display the fitted O1s peaks of CuO, CuO/TiO_2 and Ag@Cu_2O–CuO/TiO_2, respectively. As can be seen in Fig. 4(b), the O1s spectra of CuO were deconvoluted with five peaks with binding energy positions 529.6, 530.6, 532.0, 532.7, and 533.5 eV. The peak located at the lowest binding energy of 529.6 eV is allocated to the lattice oxygen of the CuO structure [60–62]. The peak located at 530.6 eV can be assigned to the CO_3^{2-}/HCO_3^- and OH^- groups [63]. The deconvoluted XPS peak at 532.0 eV corresponds to the weakly oxidized carbon species [63,64] and the peaks at 532.7 and 533.5 eV related to the binding energy positions where weakly bound species are adsorbed [63,65,66]. For CuO/TiO_2, the deconvoluted O1s peak at 529.8 eV signifies the lattice-O of CuO and or TiO_2 [58,59,65], while the peak at 531.3 and 532.8 eV are due to surface adsorbed OH group and weakly adsorbed bound species [57–60, 63]. Similarly, the fitted O1s peaks of the sample Ag@Cu_2O–CuO/TiO_2 at 529.8, 530.3, 531.8, and 532.9 eV are ascribed to lattice-O^{2-} of CuO and or TiO_2, Ti_2O_3, or (lattice- O^{2-} of Cu_2O), weakly oxidized carbon species and adsorbed bound species, respectively [54–56,59,60,63,65]. Likewise, the fitted O1s XPS peaks of Ag@TiO_2 and Ag@CuO counterparts are displayed in Fig. S5(c), and (d) respectively in SI.

Fig. 5(a–c) illustrates the high-resolution Cu 2p XPS measurements of CuO, CuO/TiO_2, and Ag@Cu_2O–CuO/TiO_2. In CuO, the Cu 2p spectra show two distinct peaks at BE 933.8 and 953.7 eV corresponding to the Cu^{2+} state in CuO. Similarly, the Cu $2p_{3/2}$ and Cu $2p_{1/2}$ doublet was observed at 933.5 and 953.5 eV in CuO/TiO_2 [61,63,66,67]. In addition, the peak located at BE 962.2 and 962.4 eV in CuO and CuO/TiO_2, respectively, are related to a typical CuO satellite peaks. The peaks in the binding energy range of 940–945 eV in CuO are known as shake-up satellite peak (Fig. 5(b)) [61,67,70–73]. However, in Ag@Cu_2O–CuO/TiO_2, the Cu 2p spectrum can be fitted with seven peaks at B.E. 932.5, 933.8, 941.3, 943.8, 952.4, 953.8 and 962.3 eV (Fig. 5(c)). The peaks at 933.8 and 953.8 eV are attributed to $2p_{3/2}$ and $2p_{1/2}$ peaks

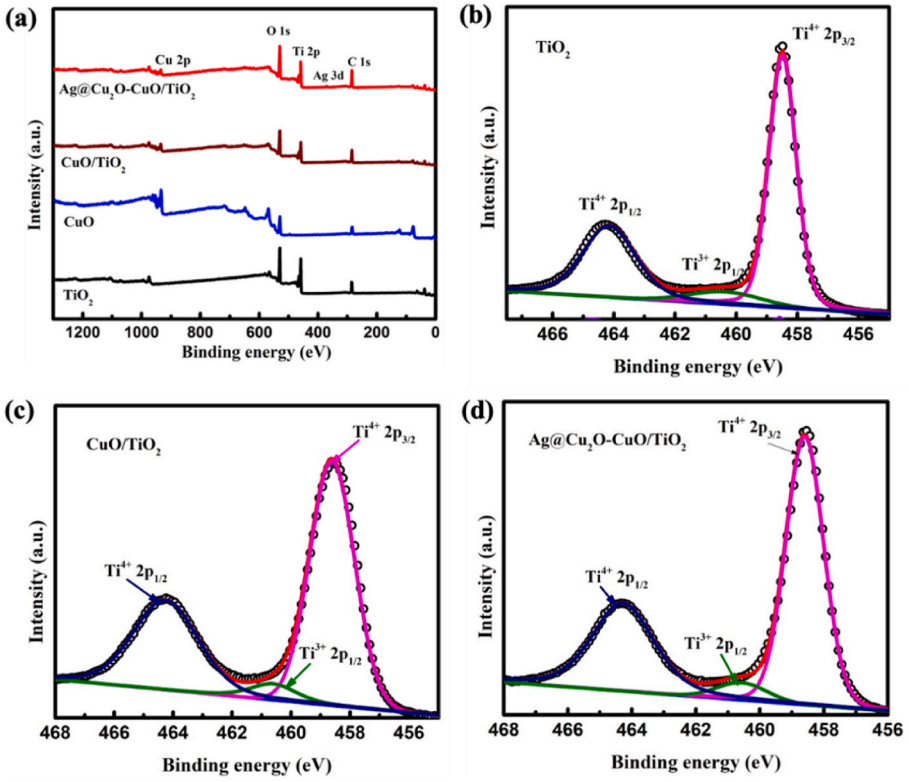

Fig. 3. (a) XPS measurements (Full survey profile) of various catalysts. XPS peak fitting: Ti 2p spectra of (b) TiO_2, (c) CuO/TiO_2, and (d) Ag@Cu_2O–CuO/TiO_2

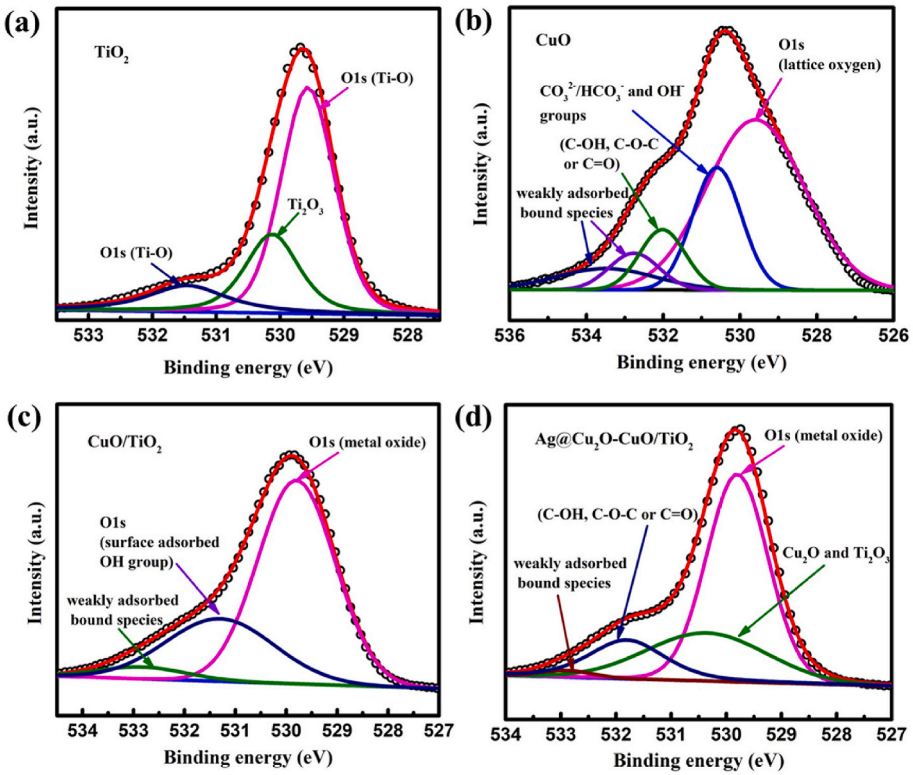

Fig. 4. XPS peak fitting: O 1s spectra of (a) TiO_2, (b) CuO, (c) CuO/TiO_2, and (d) $Ag@Cu_2O–CuO/TiO_2$.

of Cu^{2+}. Notably, the additional peaks at 932.5 and 952.4 eV representing Cu $2p_{3/2}$ and Cu $2p_{1/2}$ peaks suggest the presence of Cu_2O (Cu^{1+} oxidation state) in $Ag@Cu_2O–CuO/TiO_2$ [60,67–70]. This result validates the findings of the Raman and ESR studies. The ratio of the area of Cu $2p_{3/2}$ peak for Cu_2O and CuO in the XPS spectra of $Ag@Cu_2O–CuO/TiO_2$ was calculated to be 10:27 and the ratio of the area of Cu $2p_{1/2}$ for the same was found to be 10:18 showing that CuO is larger in quantity than Cu_2O. The areas of shake-up satellites and satellite peaks are decreased in $Ag@Cu_2O–CuO/TiO_2$, which could be due to the presence of Ag that retards the complete transformation from Cu_2O to CuO. However, the high-resolution Cu 2p spectrum of the Ag@CuO sample shown in Fig. S5(b) reveals only the Cu^{2+} oxidation state. Furthermore, the well-resolved XPS spectrum of Ag 3d of the $Ag@Cu_2O–CuO/TiO_2$ photocatalyst is shown in Fig. 5(d). The Ag 3d doublet at 368.5 ($3d_{5/2}$) and 374.5 ($3d_{3/2}$) eV is due to the spin-orbit splitting, and exhibits an energy separation of 6.0 eV, indicating the presence of metallic Ag [74–76]. Similar results were evidenced in $Ag@TiO_2$ and Ag@CuO, shown in Figs. S6(a) and S6(b), respectively.

The valence band XPS spectra of TiO_2, CuO and Cu_2O were recorded to determine the valence band maximum (VBM) and comprehend the band edge positions of the heterojunctions [31]. The VBM of pristine TiO_2 was found to be 2.52 eV, determined by linear extrapolation of the curve as shown in Fig. 5(e). Likewise, the VBM of CuO and Cu_2O was calculated to be 1.02 eV and 0.65 eV, respectively. Thus, considering the bandgap value obtained from Tauc plot (shown in Fig. 1(d)), the conduction band minimum (CBM) of the photocatalysts were estimated to be −0.5, −0.45, and −1.36 eV for TiO_2, CuO and Cu_2O.

3.4. FE-SEM and TEM analysis

The surface morphologies of Ag, TiO_2, CuO, CuO/TiO_2, and $Ag@Cu_2O–CuO/TiO_2$ were characterized by FE-SEM, shown in Fig. 6 (a–f). The formation of the bulbous branched structure of Ag is displayed in Fig. 6(a and b) at different magnifications. The TiO_2 nanoparticles are observed to be agglomerated, with an average size of 50 nm (Fig. 6(c)). The SEM micrograph of pure CuO shows a spherical structure of sizes 500–900 nm (shown in Fig. 6(d)). However, this spherical shape is no longer observed in CuO/TiO_2 and $Ag@Cu_2O–CuO/TiO_2$, which is possibly due to the higher amount of TiO_2 matrix than CuO. Similar morphology was observed in CuO/TiO_2 and $Ag@Cu_2O–CuO/TiO_2$, as shown in Fig. 6(e) and (f).

In addition, the TEM images of Ag, TiO_2, CuO/TiO_2, and $Ag@Cu_2O–CuO/TiO_2$ were analyzed to obtain further morphostructural information. The bulbous branched structure of Ag is shown in Fig. 7(a). The magnified view of the bulbous branched structure of Ag is displayed in Fig. 7(b) with highlighted dotted lines. A uniform distribution of the spherical-shaped pure CuO was evidenced with average sizes of 0.9 μm, shown in Fig. 7(d). The TEM image of TiO_2, CuO/TiO_2, and $Ag@Cu_2O–CuO/TiO_2$ are presented in Fig. 7(c), (f), and (h), respectively, and show similar morphological characteristics. The obtained size of the TiO_2 nanoparticles ranged from 30 to 50 nm. The interplanar spacing (*d*) of CuO, calculated from the HR-TEM micrograph shown in Fig. 7(e), was found to be 0.25 nm. The HR-TEM of CuO/TiO_2 in Fig. 7(g), reveals the presence of two different interplanar spacings, 0.25 and 0.32 nm, which correspond to CuO and TiO_2, respectively. Furthermore, the obtained interplanar spacings 0.2, 0.24, 0.25, and 0.32 nm in $Ag@Cu_2O–CuO/TiO_2$ sample (shown in Fig. 7 (i)), indicated the existence of Ag, Cu_2O, CuO, and TiO_2, respectively.

3.5. Photoelectrochemical experiments

The photoelectrochemical experiments were performed in an electrochemical cell consisting three-electrode system with 1 M NaOH electrolyte solution. The photocatalysts were deposited on FTO substrate, which served as the working electrode. A platinum wire was used as the counter electrode, while Ag/AgCl served as the reference electrode. Fig. 8(a) shows the current-voltage (I–V) characteristics of TiO_2, CuO, CuO/TiO_2, and $Ag@Cu_2O–CuO/TiO_2$ under visible light illumination. The pristine TiO_2 and CuO shows negligible current, whereas the CuO/TiO_2 composite exhibits a small photocurrent density of 0.8 μA/

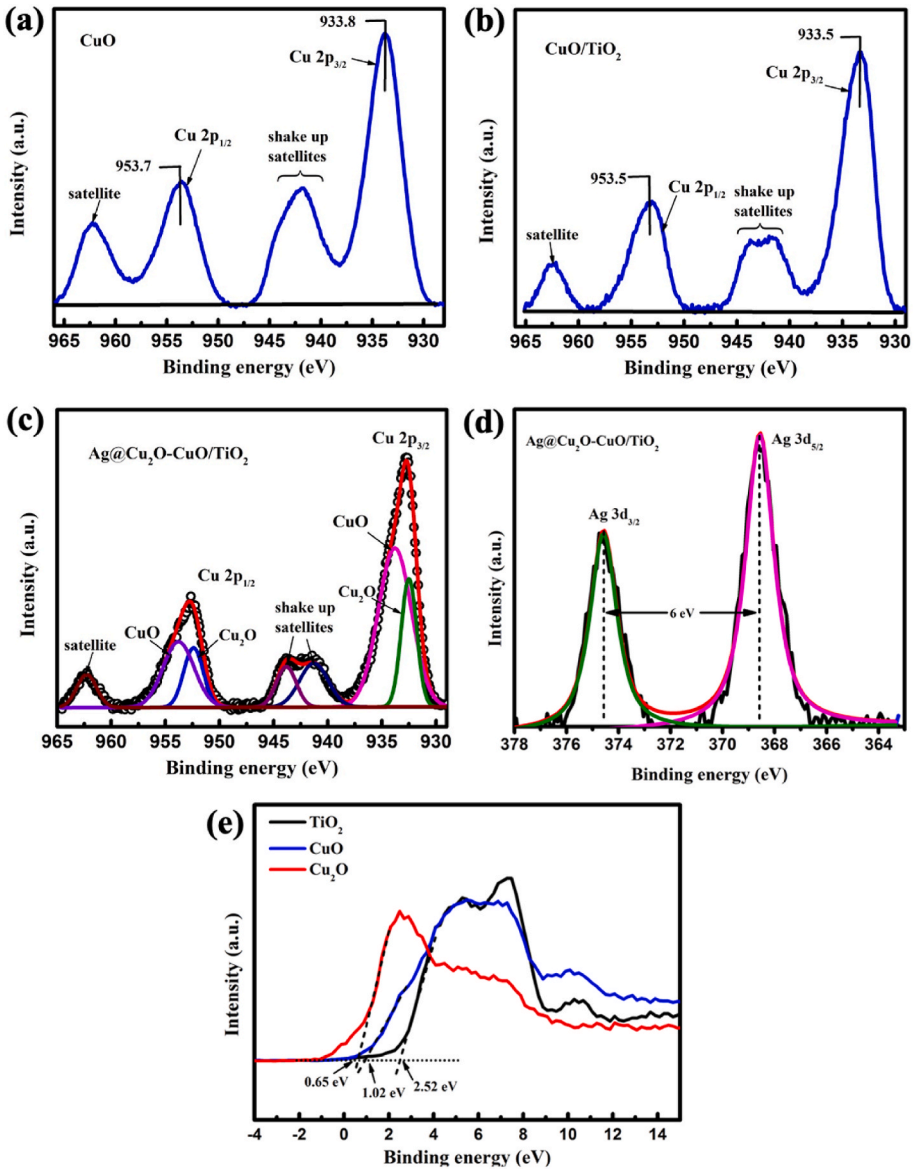

Fig. 5. XPS peak fitting Cu 2p spectra of (a) CuO (b) CuO/TiO_2, (c) $Ag@Cu_2O–CuO/TiO_2$, (d) XPS scanning of Ag 3 d, and (e) valence band XPS spectra of TiO_2, CuO and Cu_2O.

cm^2. However, the $Ag@Cu_2O–CuO/TiO_2$ photocatalyst display substantial increase in the photocurrent density up to 2.6 $\mu A/cm^2$. This result suggests that there is an increase and transfer of photogenerated charge carriers resulting from the plasmonic enhancement in the light absorption and multi-heterojunctions. In addition, a lower resistance in charge carrier transfer was evident from the electrochemical impedance spectroscopy (EIS) measurement of the $Ag@Cu_2O–CuO/TiO_2$ photocatalyst, shown in Fig. S10 of SI [30]. The photo-chronoamperometric experiment using TiO_2, CuO, CuO/TiO_2, and $Ag@Cu_2O–CuO/TiO_2$ photocatalysts was perfumed at 0.5 V vs. Ag/AgCl electrode. A set of three repeated cycle of lights on and off state for approximately 40 and 30 s, respectively, was displayed in Fig. 8(b). The $Ag@Cu_2O–CuO/TiO_2$ photocatalyst exhibited substantial photocurrent density, up to 14 times higher compared to the TiO_2 counterpart.

3.6. Photocatalytic degradation kinetics

To evaluate the photocatalytic activity of the photocatalysts, the kinetic study of MB degradation was performed. Fig. 9(a) illustrates the degradation profile of MB from 0 to 60 min irradiation of visible light. A maximum degradation was shown by $Ag@Cu_2O–CuO/TiO_2$ with a degradation percentage of 83%, while the CuO/TiO_2, CuO, and TiO_2 photocatalysts exhibited 26, 6.4, and 5.9%, respectively. The absorption spectra of MB degradation using various photocatalysts was shown in Figs. S7(a–d). The rate of degradation of MB was calculated from ln C/Co vs. time graph as plotted in Fig. 9(b). The degradation followed pseudo-first-order kinetics with a good regression coefficient. The degradation rate by $Ag@Cu_2O–CuO/TiO_2$ photocatalyst was found 26.5 times higher than the pure TiO_2. Table 1 displays the calculated rate constants of MB degradation by different photocatalysts and regression coefficients of the linear fit. The degradation trend and the rate constant determination of the counterparts $Ag@TiO_2$ and Ag@CuO are displayed in Figs. S8(a–b). In addition, the degradation of phenol using the photocatalysts was performed under a similar experimental setup and light illumination (shown in Fig. S9 in SI). It was observed that the $Ag@Cu_2O–CuO/TiO_2$ photocatalyst exhibited 5 times more activity than the pristine titania.

It was observed that the CuO/TiO_2 photocatalyst also exhibits a significant improvement in MB degradation compared to pure TiO_2. This enhancement is likely due to the electron-hole separation due to the

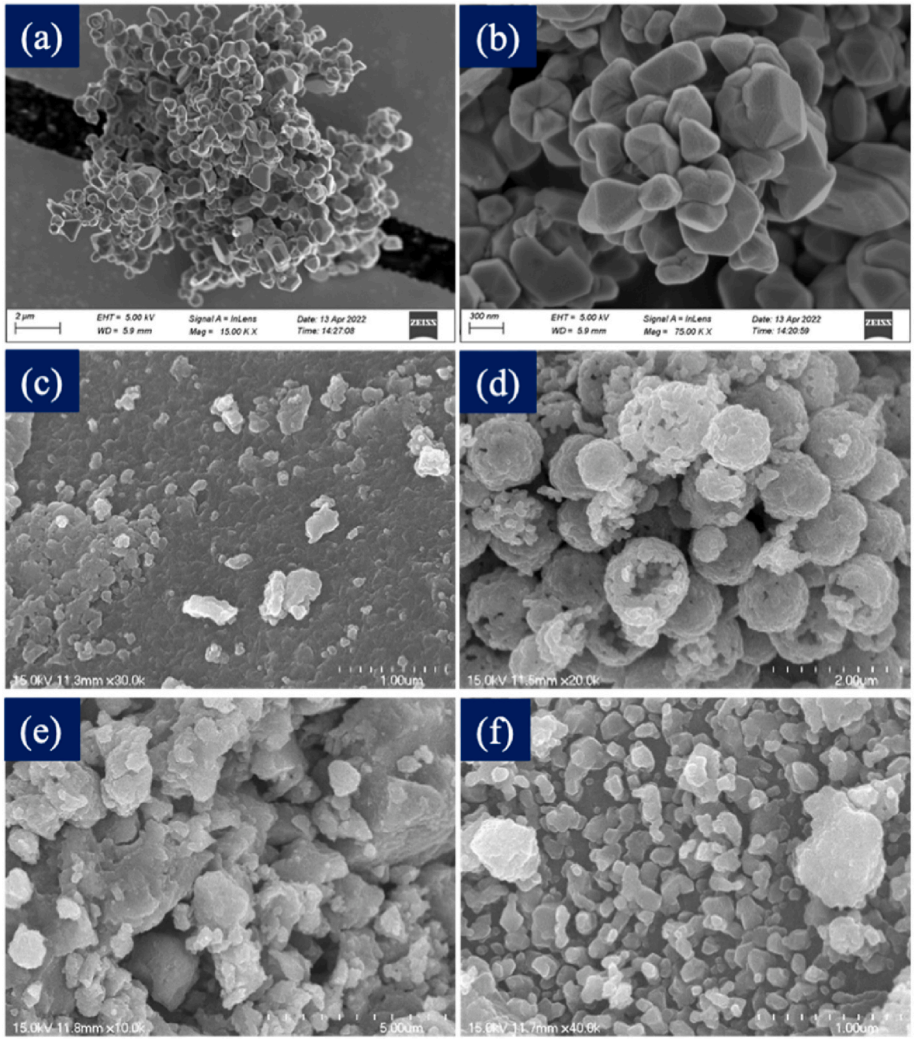

Fig. 6. FE-SEM image of (a–b) Ag, (c) TiO_2, (d) CuO, (e) CuO/TiO_2 and (f) $Ag@Cu_2O–CuO/TiO_2$.

built-in electric field at the interface that prolongs the lifetime of charge carriers for photocatalytic reactions [16,77]. Notably, the activity was further enhanced by $Ag@Cu_2O–CuO/TiO_2$ photocatalyst. The SPR effect of bulbous Ag nanostructure amplifies the localized electric field in their vicinity, increasing charge carrier generation and facilitating effective separation between them [19]. Due to the shape effect of the plasmonic nanostructures, the particular bulbous branched structure of Ag exhibits low symmetry, allowing for extensive absorption over the visible spectrum [35,36,78]. In addition, the Ag nanoparticle acts as an electron source, which promotes the electron injection into the CB of the semiconductors under visible light illumination [19]. The recyclability test was carried out to evaluate the stability of the primary photocatalyst $Ag@Cu_2O–CuO/TiO_2$ under the similar experimental set-up and the light source, shown in Fig. 10(a). The recyclability test was conducted over four cycles of 60 min each and after the first cycle, remanent MB concentration was made equal to the initial value (at 0 min). The fall in the photocatalytic activity after fourth cycle was extremely minimal, displayed in Fig. 10(b) (less than 15%), indicating the high stability and robustness of the photocatalyst.

3.7. Active radical quenching experiments

To understand about the active species involved in the degradation of MB, free radical quenching experiments were conducted for the main photocatalyst $Ag@Cu_2O–CuO/TiO_2$, shown in Fig. 11(a). The major reactions that occur in the photocatalytic process are shown in Eqs. (1)–(9) [31,79]. It was observed that there is a significant drop in the order SN > LH > AO, in MB degradation when the SN (e^- quencher), LH ($^1O_2$ quencher), and AO (h^+ quencher) was introduced, shown in Fig. 11(b). This result indicates the major participation of e^-, $^1O_2$ and h^+ in the degradation process. The calculated rate constants are shown in Table 2. On the other hand, there is only a small decline in the degradation with the addition of BQ ($^{\bullet}O_2^-$ quencher) and IPA ($^{\bullet}OH$ quencher), up to 4.3% and 1%, respectively. However, to ensure the role of $^{\bullet}O_2^-$ and $^{\bullet}OH$ radicals, double-quenching test was performed using BQ and IPA simultaneously. Clearly, a substantial drop in the degradation was observed in double-quenching, which indicates that $^{\bullet}O_2^-$ and $^{\bullet}OH$ radicals are produced abundantly by e^- and h^+ (as shown in Eqs. (2)–(7)) and therefore individual quenching is not sufficient using BQ and IPA [80]. It can be speculated that, during $^{\bullet}O_2^-$ quenching by BQ, the production of $^{\bullet}OH$ (by both e^- and h^+) is sufficient to take part in the degradation reaction and therefore no significant decline in the degradation can be observed. Likewise, $^{\bullet}OH$ quenching by IPA was supressed by $^{\bullet}O_2^-$ production. In addition, the double-quenching experiment using LH and SN demonstrates lowest degradation of MB, implying the active participation of both e^-, and $^1O_2$.

Summarily, when the scavenging agent SN and AO capture e^- and h^+, respectively, it prevents the formation of $^{\bullet}O_2^-$, $^{\bullet}OH$, and $^1O_2$, resulting substantial decline in the degradation. The possible degradation pathways of MB and the possible intermediates are discussed in the SI

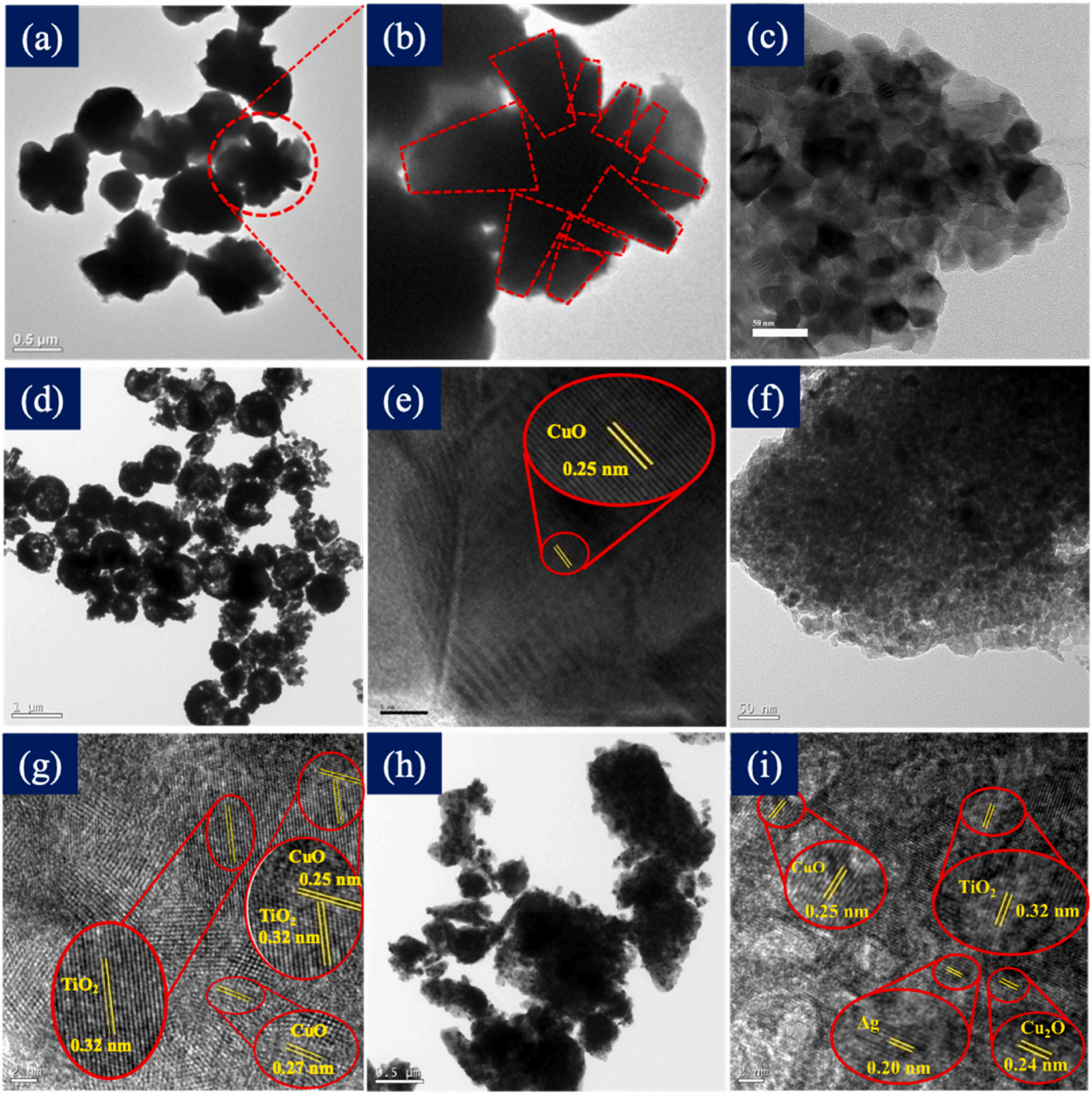

Fig. 7. TEM and HR-TEM images of (a–b) Ag, (c) TiO_2, (d–e) CuO, (f–g) CuO/TiO_2 and (h–i) Ag@Cu_2O–CuO/TiO_2.

(Fig. S11).

$$Photocatalyst + h\nu \rightarrow h^+ + e^- \quad (1)$$

$$O_2 + e^- \rightarrow O_2^{\bullet -} \quad (2)$$

$$O_2^{\bullet -} + e^- + 2H^+ \rightarrow H_2O_2 \quad (3)$$

$$O_2^{\bullet -} + H_2O_2 \rightarrow \bullet OH + OH^- + O_2 \quad (4)$$

$$e^- + H_2O_2 \rightarrow \bullet OH + OH^- \quad (5)$$

$$h^+ + OH^- \rightarrow \bullet OH \quad (6)$$

$$h^+ + H_2O \rightarrow H^+ + \bullet OH \quad (7)$$

$$2 \bullet OH \rightarrow H_2O_2 \quad (8)$$

$$h^+ + O_2^{\bullet -} \rightarrow {}^1O_2 \quad (9)$$

3.8. Photocatalytic mechanism and its schematic representation

As indicated by valence band XPS analysis and the Tauc plot, the conduction band minimum (CBM) of TiO_2 situated below the CBM of Cu_2O, whereas the valence band maximum (VBM) of TiO_2 lies much below than that of Cu_2O, forming a type-II (staggered gap) band alignment between TiO_2 and Cu_2O. Likewise, the CBM and VBM levels of CuO

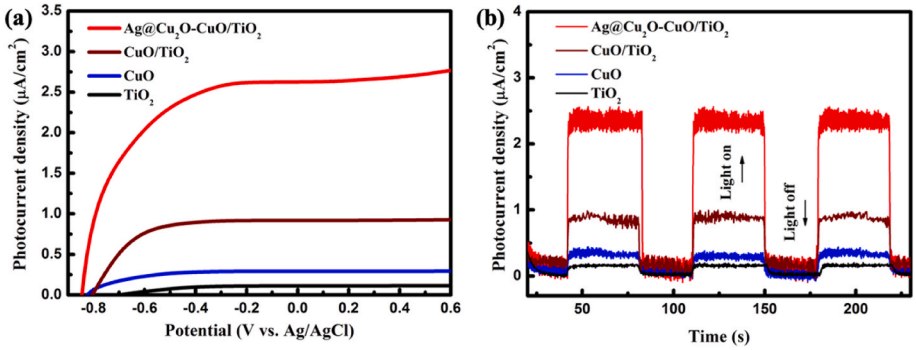

Fig. 8. (a) Photocurrent density vs. voltage (I–V) characteristics under visible light illumination, and (b) Photo-chronoamperometric results of TiO_2, CuO, CuO/TiO_2, and $Ag@Cu_2O–CuO/TiO_2$.

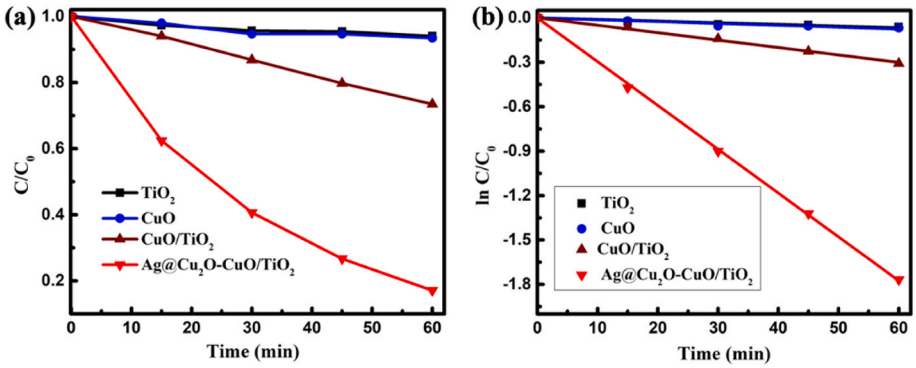

Fig. 9. (a) Photocatalytic degradation profile (C/C_o vs. time) of MB under visible light using different photocatalysts (b) ln C/C_o vs. time plot to determine the rate constant.

Table 1
Rate of degradation of MB using different photocatalysts under visible light.

Photocatalyst	Rate constant (h^{-1})	Regression coefficient (R^2)
TiO_2	0.067	0.961
CuO	0.076	0.959
CuO/TiO_2	0.301	0.997
$Ag@Cu_2O–CuO/TiO_2$	1.774	0.999

are situated between the CBM and VBM position of TiO_2, resulting a type-I (straddling gap) heterojunction. Fig. 12 illustrates the ternary heterojunction system, where a type-I heterojunction exists between CuO with TiO_2, while a type-II heterojunction is present between Cu_2O and TiO_2. The Ag nanoparticles are considered to be in contact with CuO, Cu_2O, and TiO_2. The unique branching shape of the Ag microstructure obtained in this study enables electromagnetic wave to stimulate multiple resonances in the nanoparticles resulting broad absorption of the visible light spectra [26,35]. The facets of Ag nanoparticles, revealed from FE-SEM image, can establish excellent contact with CuO and TiO_2, forming a Schottky junction that effectively separates photogenerated charge carriers [81].

When the photocatalyst is illuminated by light, the semiconductors CuO, Cu_2O, and TiO_2 generate electron-hole pairs, and the electrons in the Ag metal exhibit local surface plasmonic resonance [82–84]. As depicted in Fig. 12, the photo-excited electrons at the CB of the Cu_2O phase are first transferred to the CB of TiO_2 and subsequently to the CB of CuO. On the other hand, the holes generated at the VB of TiO_2 migrate towards the VB of CuO and Cu_2O. However, the holes that are transferred to the VB of Cu_2O are unable to produce reactive species as its position is unsuitable for oxidation reactions (indicated with cross mark in Fig. 12). Besides, the SPR promotes electron injection from Ag

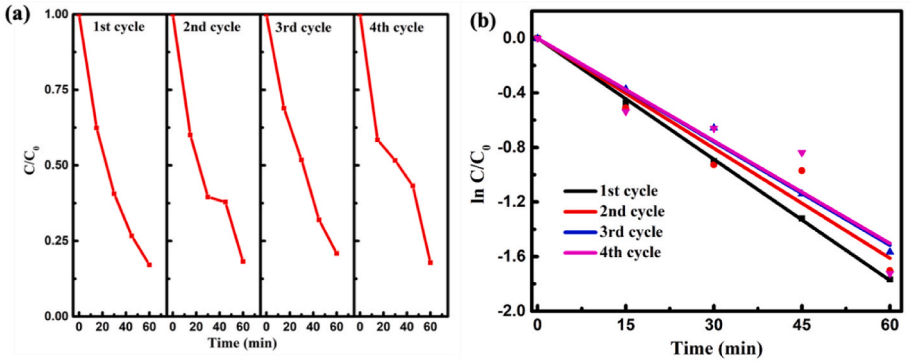

Fig. 10. (a) Recyclability test of $Ag@Cu_2O–CuO/TiO_2$ photocatalyst, and (b) ln C/C_o vs. time plot to determine the rate constant.

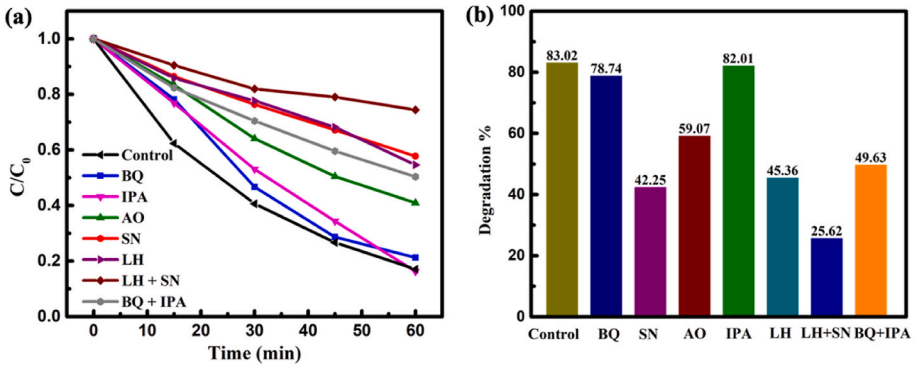

Fig. 11. (a) Photocatalytic degradation of MB and (b) degradation percent by Ag@Cu_2O–CuO/TiO_2 photocatalyst with various scavenging agents.

Table 2
Quenching agents, amount, active radicals, and rate constants.

Quenching agent	Amount	Active radical (s)	Rate constant (h^{-1})
SN	4 mM	e^-	0.54
LH	0.5 mM	$^1O_2$	0.56
AO	4 mM	h^+	0.88
BQ	0.5 mM	$^\bullet O_2^-$	1.56
IPA	1 mL	$^\bullet OH$	1.59
BQ + IPA	0.5 mM + 1 mL	$^\bullet O_2^-$ and $^\bullet OH$	0.55
SN + LH	4 mM + 0.5 mM	e^- and $^1O_2$	0.32

nanoparticles, leading to a higher population of electron at the conduction bands of TiO_2, CuO, and Cu_2O, which ensures the adequate availability of charge carriers for photocatalytic reactions [19]. These electrons are the outcome of plasmonic excitations induced by the time-dependent electric field of illuminating light in the visible range. Consequently, the photogenerated electrons and holes undergo a large spatial separation and migrate towards the surface of the photocatalyst and participate in chemical reactions with the adsorbed molecules to produce active radicals [9,85].

4. Conclusion

In summary, we report the synthesis of a novel plasmonic-heterojunction photocatalyst (Ag@Cu_2O–CuO/TiO_2) with extensive visible light absorption and high photocatalytic activity. XRD and XPS measurements corroborated the crystalline phases of CuO and TiO_2, chemical compositions, and the presence of metallic Ag. The asymmetrical feature of bulbous branched Ag, confirmed in the FE-SEM analysis, results in SPR induced light absorption across the visible and near-infrared region. The photocatalytic activity of the Ag@Cu_2O–CuO/TiO_2 photocatalyst was found to be 26.5 times higher than the pristine TiO_2 counterpart towards methylene blue degradation without sacrificial reagents. The increased photoactivity of Ag@Cu_2O–CuO/TiO_2 photocatalyst can be attributed to the synergistic impact of reduced electron-hole pair recombination caused by the Cu_2O–CuO/TiO_2 ternary heterojunction, strong visible light absorption, and SPR driven enhanced localized field by Ag. In addition, the presence of the mixed phase of TiO_2 in Ag@Cu_2O–CuO/TiO_2 facilitates interfacial charge separation between the phases. Remarkably, the photocatalyst exhibited exceptional recyclability, indicating its excellent stability and robustness for efficient photocatalytic applications. The current study suggests that the heterojunction-plasmonic nanostructured photocatalyst substantially enhances the photocatalytic efficiency synergistically and shows great potential for dye-contaminated water treatments.

CRediT author statement

R. Basumatary: Visualization, Methodology, Investigation, Formal analysis, Writing-original draft. **D. Konwar**: Characterization, Investigation, **B. Basumatary**: Formal analysis, Investigation. **A. Ramchiary**: Conceptualization, Methodology, Writing-Review & editing, Supervision, Project administration, Funding acquisition.

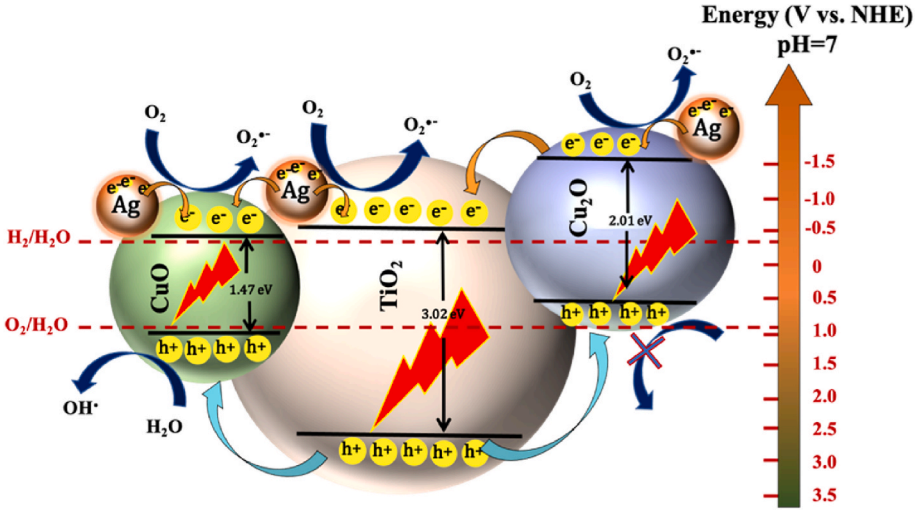

Fig. 12. Photocatalytic mechanism of Ag@Cu_2O–CuO/TiO_2 photocatalyst: interfacial junctions between CuO–TiO_2–Cu_2O phase.

Declaration of competing interest

The authors declare that they have no known competing financial interests or personal relationships that could have appeared to influence the work reported in this paper.

Data availability

Data will be made available on request.

Acknowledgement

We acknowledge the support by the Science and Engineering Research Board (SERB), New Delhi, India, for the research grant (grant no: EEQ/2019/000461). The authors would also like to thank SAIC, IASST Guwahati (Under DST, GoI) and CIF at IITG for their help with sample characterizations.

Appendix A. Supplementary data

Supplementary data to this article can be found online at https://doi.org/10.1016/j.jpcs.2023.111435.

References

[1] D. Swami, D. Buddhi, Removal of contaminants from industrial wastewater through various non-conventional technologies, Int. J. Environ. Pollut. 27 (2006) 324–346.
[2] R. Al-Tohamy, S.S. Ali, F. Li, K.M. Okasha, Y.A.G. Mahmoud, T. Elsamahy, H. Jiao, Y. Fu, J. Sun, A critical review on the treatment of dye-containing wastewater: ecotoxicological and health concerns of textile dyes and possible remediation approaches for environmental safety, Ecotoxicol. Environ. Saf. 231 (2022), 113160.
[3] P.C. Nagajyothi, S.V. Prabhakar Vattikuti, K.C. Devarayapalli, K. Yoo, J. Shim, T.V. M. Sreekanth, Green synthesis: photocatalytic degradation of textile dyes using metal and metal oxide nanoparticles-latest trends and advancements, Crit. Rev. Environ. Sci. Technol. 50 (2020) 2617–2723.
[4] H. Zhang, D. Yu, W. Wang, P. Gao, L. Zhang, S. Zhong, B. Liu, Construction of a novel BON-Br-AgBr heterojunction photocatalysts as a direct Z-scheme system for efficient visible photocatalytic activity, Appl. Surf. Sci. 497 (2019), 143820.
[5] Q.P. Zhang, J. Li, M. Xu, Ag decorated ZnO based nanocomposites for visible light-driven photocatalytic degradation: basic understanding and outlook, J. Phys. D 55 (2022) 483001.
[6] D. Konwar, P. Basumatary, S.P. Woo, Y. Lee, Y.S. Yoon, Enhanced performance for proton conducting fuel cells at low temperature, Electrochim. Acta 290 (2018) 142–149.
[7] G. Li, Y. Wang, L. Mao, Recent progress in highly efficient Ag-based visible-light photocatalysts, RSC Adv. 4 (2014) 53649–53661.
[8] S.J. Moniz, S.A. Shevlin, D.J. Martin, Z.X. Guo, J. Tang, Visible-light driven heterojunction photocatalysts for water splitting–a critical review, Energy Environ. Sci. 8 (2015) 731–759.
[9] S. Banerjee, S.C. Pillai, P. Falaras, K.E. O'shea, J.A. Byrne, D.D. Dionysiou, New insights into the mechanism of visible light photocatalysis, J. Phys. Chem. Lett. 5 (2014) 2543–2554.
[10] Y. Wang, Q. Wang, X. Zhan, F. Wang, M. Safdar, J. He, Visible light driven type II heterostructures and their enhanced photocatalysis properties: a review, Nanoscale 5 (2013) 8326–8339.
[11] C. Chen, M. Shen, Y. Li, One pot synthesis of 1T@2H-MoS_2/SnS_2 heterojunction as a photocatalyst with excellent visible light response due to multiphase synergistic effect, Chem. Phys. 548 (2021), 111230.
[12] Q. Jin, X. Dai, J. Song, K. Pu, X. Wu, J. An, T. Zhao, High photocatalytic performance of g-C_3N_4/WS_2 heterojunction from first principles, Chem. Phys. 545 (2021), 111141.
[13] H. Zhang, Y. Xiao, L. Tian, Y. Tang, X. Liu, Z. Shi, Z. Wu, Z. Wei, In-situ fabrication of a phase continuous transition Bismuth iodide/Bismuth niobate heterojunction: interface regulation and the enhanced photodegradation mechanism, Chem. Phys. 562 (2022), 111644.
[14] Y. Li, T. Cao, Z. Mei, X. Li, D. Sun, Separating type I heterojunction of NaBi$(MoO_4)_2$/Bi_2MoO_6 by TiO_2 nanofibers for enhanced visible-photocatalysis, Chem. Phys. (2020) 533 110696.
[15] G. Li, Y. Cai, X. Wang, L. Zhang, Q. Xie, P. Chen, C. Li, J. Sun, T. Li, L. Dong, Direct Z-scheme heterojunction rutile-TiO_2/g-C_3N_4 catalyst constructed by solid grinding method for photocatalysis degradation, Chem. Phys. 559 (2022), 111558.
[16] R. Zhou, S. Yang, E. Tao, L. Liu, J. Qian, The defect is perfect: MoS_2/TiO_2 modified with unsaturated Mo vacancies to construct Z-scheme heterojunction & improve mobility of e, J. Clean. Prod. 337 (2022), 130511.
[17] B. Basumatary, R. Basumatary, A. Ramchiary, D. Konwar, Evaluation of Ag@ TiO_2/WO_3 heterojunction photocatalyst for enhanced photocatalytic activity towards methylene blue degradation, Chemosphere 286 (2022), 131848.
[18] X. Zhang, L. Wang, C. Liu, Y. Ding, S. Zhang, Y. Zeng, S. Luo, A bamboo-inspired hierarchical nanoarchitecture of Ag/CuO/TiO_2 nanotube array for highly photocatalytic degradation of 2, 4-dinitrophenol, J. Hazard Mater. 313 (2016) 244–252.
[19] X. Zhang, Y.L. Chen, R.S. Liu, D.P. Tsai, Plasmonic photocatalysis, Rep. Prog. Phys. 76 (2013), 046401.
[20] J. Ji, Z. Li, W. Sun, H. Wang, Thermal annealing induced tunable localized surface plasmon resonance of Au/Ag bimetallic thin film, Chem. Phys. 541 (2021), 111034.
[21] C. An, S. Wang, Y. Sun, Q. Zhang, J. Zhang, C. Wang, J. Fang, Plasmonic silver incorporated silver halides for efficient photocatalysis, J. Mater. Chem. 4 (2016) 4336–4352.
[22] M.J. Nalbandian, M. Zhang, J. Sanchez, S. Kim, Y.H. Choa, D.M. Cwiertny, N. V. Myung, Synthesis and optimization of Ag–TiO_2 composite nanofibers for photocatalytic treatment of impaired water sources, J. Hazard Mater. 299 (2015) 141–148.
[23] R. Raji, K.S. Sibi, K.G. Gopchandran, ZnO: Ag nanorods as efficient photocatalysts: sunlight driven photocatalytic degradation of sulforhodamine B, Appl. Surf. Sci. 427 (2018) 863–875.
[24] B.J. Wiley, Y. Chen, J.M. McLellan, Y. Xiong, Z.Y. Li, D. Ginger, Y. Xia, Synthesis and optical properties of silver nanobars and nanorice, Nano Lett. 7 (2007) 1032–1036.
[25] C.M. Cobley, M. Rycenga, F. Zhou, Z.Y. Li, Y. Xia, Controlled etching as a route to high quality silver nanospheres for optical studies, J. Phys. Chem. C 113 (2009) 16975–16982.
[26] B.J. Wiley, S.H. Im, Z.Y. Li, J. McLellan, A. Siekkinen, Y. Xia, Maneuvering the surface plasmon resonance of silver nanostructures through shape-controlled synthesis, J. Phys. Chem. B 110 (2006) 15666–15675.
[27] R. Gang, Y. Xia, L. Xu, L. Zhang, S. Ju, Z. Wang, S. Koppala, Size controlled Ag decorated TiO_2 plasmonic photocatalysts for tetracycline degradation under visible light, Surface. Interfac. 31 (2022), 102018.
[28] Y. Tian, T. Tatsuma, Mechanisms and applications of plasmon-induced charge separation at TiO_2 films loaded with gold nanoparticles, J. Am. Chem. Soc. 127 (2005) 7632–7637.
[29] N.L. Gavade, S.B. Babar, A.N. Kadam, A.D. Gophane, K.M. Garadkar, Fabrication of M@Cu_xO/ZnO (M= Ag, Au) heterostructured nanocomposite with enhanced photocatalytic performance under sunlight, Ind. Eng. Chem. Res. 56 (2017) 14489–14501.
[30] C. Yue, C. Zhu, W. Zheng, J. Qiu, Z. Du, C. Ling, F.Q. Liu, Plasmonic Bi NP-accelerated interfacial charge transfer for enhanced solar-driven ciprofloxacin mineralization, Environ. Sci. Nano 9 (2022) 349–360.
[31] C. Ling, C. Yue, R. Yuan, J. Qiu, F.Q. Liu, J.J. Zhu, Enhanced removal of sulfamethoxazole by a novel composite of TiO_2 nanocrystals in situ wrapped-Bi_2O_4 microrods under simulated solar irradiation, Chem. Eng. J. 384 (2020), 123278.
[32] C. Yu, H. He, W. Zhou, Z. Liu, L. Wei, Novel rugby-ball-like $Zn_3(PO_4)_2$@C_3N_4 photocatalyst with highly enhanced visible-light photocatalytic performance, Sep. Purif. Technol. 217 (2019) 137–146.
[33] A. Ramchiary, S.K. Samdarshi, Ag deposited mixed phase titania visible light photocatalyst–Superiority of Ag-titania and mixed phase titania co-junction, Appl. Surf. Sci. 305 (2014) 33–39.
[34] Y. Zhu, K. Mimura, M. Isshiki, Oxidation mechanism of Cu_2O to CuO at 600–1050 C, Oxid. Metals 62 (2004) 207–222.
[35] Y. Wang, P.H. Camargo, S.E. Skrabalak, H. Gu, Y. Xia, A facile, water-based synthesis of highly branched nanostructures of silver, Langmuir 24 (2008) 12042–12046.
[36] M. Rycenga, C.M. Cobley, J. Zeng, W. Li, C.H. Moran, Q. Zhang, D. Qin, Y. Xia, Controlling the synthesis and assembly of silver nanostructures for plasmonic applications, Chem. Rev. 111 (6) (2011) 3669–3712.
[37] L. Samet, J.B. Nasseur, R. Chtourou, K. March, O. Stephan, Heat treatment effect on the physical properties of cobalt doped TiO_2 sol–gel materials, Mater. Char. 85 (2013) 1–12.
[38] B.R. Bade, S. Rondiya, S.R. Bhopale, N.Y. Dzade, M.M. Kamble, A. Rokade, M. P. Nasane, M.A. More, S.R. Jadkar, A.M. Funde, Investigation of growth mechanism for highly oriented TiO_2 nanorods: the role of reaction time and annealing temperature, SN Appl. Sci. 1 (2019) 1–13.
[39] S. Challagulla, K. Tarafder, R. Ganesan, S. Roy, Structure sensitive photocatalytic reduction of nitroarenes over TiO_2, Sci. Rep. 7 (2017) 1–11.
[40] J. Singh, K. Sahu, S. Mohapatra, Thermal annealing induced evolution of morphological, structural, optical and photocatalytic properties of Ag-TiO_2 nanocomposite thin films, J. Phys. Chem. Solid. 129 (2019) 317–323.
[41] G.S. Jamila, S. Sajjad, S.A.K. Leghari, T. Mahmood, Role of nitrogen doped carbon quantum dots on CuO nano-leaves as solar induced photo catalyst, J. Phys. Chem. Solid. 138 (2020), 109233.
[42] L. Palliyaguru, U.S. Kulathunga, L.I. Jayarathna, C.D. Jayaweera, P.M. Jayaweera, A simple and novel synthetic route to prepare anatase TiO_2 nanopowders from natural ilmenite via the H_3PO_4/NH_3 process, Int. J. Miner. Metall. Mater. 27 (2020) 846–855.
[43] H. Chen, S.M. Park, J.H. Lee, X. Meng, D.W. Shin, J.B. Yoo, Large scale fabrication of single-crystal CuO nanoplatelets using a template-free hydrothermal approach, Electron. Mater. Lett. 4 (2008).
[44] S. Kumar, Influence of synthesis strategy on the formation of microspheres of self-assembled CuO rectangular nanorods and hierarchical structures of self-assembled Cu_2O nanospheres from single precursor (copper (II) acetate monohydrate) and

their structural, optical, thermal and magnetic properties, Mater. Chem. Phys. 258 (2021), 123929.
[45] L. Sinatra, A.P. LaGrow, W. Peng, A.R. Kirmani, A. Amassian, H. Idriss, O.M. Bakr, A Au/Cu_2O–TiO_2 system for photo-catalytic hydrogen production. A pn-junction effect or a simple case of in situ reduction? J. Catal. 322 (2015) 109–117.
[46] G. Yang, D. Gao, J. Zhang, J. Zhang, Z. Shi, D. Xue, Evidence of vacancy-induced room temperature ferromagnetism in amorphous and crystalline Al_2O_3 nanoparticles, J. Phys. Chem. C 115 (2011) 16814–16818.
[47] F. Zuo, L. Wang, T. Wu, Z. Zhang, D. Borchardt, P. Feng, Self-doped Ti^{3+} enhanced photocatalyst for hydrogen production under visible light, J. Am. Chem. Soc. 132 (2010) 11856–11857.
[48] Y. Liu, B. Zhang, L. Luo, X. Chen, Z. Wang, E. Wu, D. Su, W. Huang, TiO_2/Cu_2O core/ultrathin shell nanorods as efficient and stable photocatalysts for water reduction, Angew. Chem. 127 (2015) 15475–15480.
[49] P.G. Harrison, I.K. Ball, W. Azelee, W. Daniell, D. Goldfarb, Nature and surface redox properties of copper (II)-promoted cerium (IV) oxide CO-oxidation catalysts, Chem. Mater. 12 (2000) 3715–3725.
[50] T. Dhandayuthapani, R. Sivakumar, R. Ilangovan, Growth of micro flower rutile TiO_2 films by chemical bath deposition technique: study on the properties of structural, surface morphological, vibrational, optical and compositional, Surface. Interfac. 4 (2016) 59–68.
[51] G. Nabi, W. Raza, M.B. Tahir, Green synthesis of TiO_2 nanoparticle using cinnamon powder extract and the study of optical properties, J. Inorg. Organomet. Polym. Mater. 30 (2020) 1425–1429.
[52] V. Kumaravel, S. Rhatigan, S. Mathew, M.C. Michel, J. Bartlett, M. Nolan, S. C. Pillai, Mo doped TiO_2: impact on oxygen vacancies, anatase phase stability and photocatalytic activity, J. Phys. Materials 3 (2020), 025008.
[53] Q. Hua, T. Cao, H. Bao, Z. Jiang, W. Huang, Crystal-plane-Controlled surface chemistry and catalytic performance of surfactant-free Cu_2O nanocrystals, ChemSusChem 6 (2013) 1966–1972.
[54] B. Bharti, S. Kumar, H.N. Lee, R. Kumar, Formation of oxygen vacancies and Ti^{3+} state in TiO_2 thin film and enhanced optical properties by air plasma treatment, R, Sci. Rep. 6 (2016), 32355.
[55] C. Yu, D. Cai, K. Yang, C.Y. Jimmy, Y. Zhou, C. Fan, Sol–gel derived S, I-codoped mesoporous TiO_2 photocatalyst with high visible-light photocatalytic activity, J. Phys. Chem. Solid. 71 (2010) 1337–1343.
[56] F. Peng, L. Cai, L. Huang, H. Yu, H. Wang, Preparation of nitrogen-doped titanium dioxide with visible-light photocatalytic activity using a facile hydrothermal method, J. Phys. Chem. Solid. 69 (2008) 1657–1664.
[57] X. Yu, X. Fan, L. An, Z. Li, J. Liu, X. Yu, X. Fan, L. An, Z. Li, J. Liu, Facile synthesis of Ti^{3+}-TiO_2 mesocrystals for efficient visible-light photocatalysis, J. Phys. Chem. Solid. 119 (2018) 94–99, 2018.
[58] X. Zhang, L. Wang, C. Liu, Y. Ding, S. Zhang, Y. Zeng, Y. Liu, S. Luo, A bamboo-inspired hierarchical nanoarchitecture of Ag/CuO/TiO_2 nanotube array for highly photocatalytic degradation of 2, 4-dinitrophenol, J. Hazard Mater. 313 (2016) 244–252.
[59] G. Wang, Z. Fu, T. Wang, W. Lei, P. Sun, Y. Sui, B. Zou, A rational design of hollow nanocages Ag@CuO-TiO_2 for enhanced acetone sensing performance, Sensor. Actuator. B Chem. 295 (2019) 70–78.
[60] Y. Wang, Y. Lü, W. Zhan, Z. Xie, Q. Kuang, L. Zheng, Synthesis of porous Cu_2O/CuO cages using Cu-based metal–organic frameworks as templates and their gas-sensing properties, J. Mater. Chem. 3 (2015) 12796–12803.
[61] D.A. Svintsitskiy, T.Y. Kardash, O.A. Stonkus, E.M. Slavinskaya, A.I. Stadnichenko, S.V. Koscheev, A.P. Chupakhin, A.I. Boronin, In situ XRD, XPS, TEM, and TPR study of highly active in CO oxidation CuO nanopowders, J. Phys. Chem. C 117 (2013) 14588–14599.
[62] Ç. Oruç, A. Altındal, Structural and dielectric properties of CuO nanoparticles, Ceram. Int. 43 (2017) 10708–10714.
[63] D.A. Svintsitskiy, T.Y. Kardash, A.I. Boronin, Surface dynamics of mixed silver-copper oxide $AgCuO_2$ during X-ray photoelectron spectroscopy study, Appl. Surf. Sci. 463 (2019) 300–309.
[64] A. Ganguly, S. Sharma, P. Papakonstantinou, J. Hamilton, Probing the thermal deoxygenation of graphene oxide using high-resolution in situ X-ray-based spectroscopies, J. Phys. Chem. C 115 (2011) 17009–17019.
[65] J. Yuan, J. Zhang, M.P. Yang, W.J. Meng, H. Wang, J.X. Lu, CuO nanoparticles supported on TiO_2 with high efficiency for CO_2 electrochemical reduction to ethanol, Catalysts 8 (2018) 171.
[66] R. Yang, L. Yang, T. Tao, F. Ma, M. Xu, Z. Zhang, Contrastive study of structure and photocatalytic performance with three-dimensionally ordered macroporous CuO–TiO_2 and CuO/TiO_2, Appl. Surf. Sci. 288 (2014) 363–368.
[67] Q. Zhang, L. Huang, S. Kang, C. Yin, Z. Ma, L. Cui, Y. Wang, CuO/Cu_2O nanowire arrays grafted by reduced graphene oxide: synthesis, characterization, and application in photocatalytic reduction of CO_2, RSC Adv. 7 (2017) 43642–43647.
[68] L.I. Ibarra-Rodríguez, A.M. Huerta-Flores, L.M. Torres-Martínez, Development of $Na_2Ti_6O_{13}$/CuO/Cu_2O heterostructures for solar photocatalytic production of low-carbon fuels, Mater. Res. Bull. 122 (2020), 110679.
[69] C. Shifu, Z. Sujuan, L. Wei, Z. Wei, Study on the photocatalytic activity of p–n junction photocatalyst Cu_2O/TiO_2, J. Nanosci. Nanotechnol. 9 (2009) 4397–4403.
[70] D.A. Svintsitskiy, A.I. Stadnichenko, D.V. Demidov, S.V. Koscheev, A.I. Boronin, Investigation of oxygen states and reactivities on a nanostructured cupric oxide surface, Appl. Surf. Sci. 257 (2011) 8542–8549.
[71] A.A. Ogwu, T.H. Darma, A reactive magnetron sputtering route for attaining a controlled core-rim phase partitioning in Cu_2O/CuO thin films with resistive switching potential, J. Appl. Phys. 113 (2013), 183522.
[72] I.H. Chowdhury, S. Ghosh, S. Basak, M.K. Naskar, Mesoporous CuO-TiO_2 microspheres for efficient catalytic oxidation of CO and photodegradation of methylene blue, J. Phys. Chem. Solid. 104 (2017) 103–110.
[73] X.H. Xia, Y. Gao, Z. Wang, Z.J. Jia, Structure and photocatalytic properties of copper-doped rutile TiO_2 prepared by a low-temperature process, J. Phys. Chem. Solid. 69 (2008) 2888–2893.
[74] X. You, F. Chen, J. Zhang, M. Anpo, A novel deposition precipitation method for preparation of Ag-loaded titanium dioxide, Catal. Lett. 102 (2005) 247–250.
[75] H. Zhang, C. Liang, J. Liu, Z. Tian, G. Wang, W. Cai, Defect-mediated formation of Ag cluster-doped TiO_2 nanoparticles for efficient photodegradation of pentachlorophenol, Langmuir 28 (2012) 3938–3944.
[76] S.K. Pandey, M.K. Tripathi, V. Ramanathan, P.K. Mishra, D. Tiwary, Highly facile Ag/NiO nanocomposite synthesized by sol-gel method for mineralization of rhodamine B, J. Phys. Chem. Solid. 159 (2021), 110287.
[77] K. Ding, D. Yu, W. Wang, P. Gao, B. Liu, Fabrication of multiple hierarchical heterojunction Ag@AgBr/$BiPO_4$/r-GO with enhanced visible-light-driven photocatalytic activities towards dye degradation, Appl. Surf. Sci. 445 (2018) 39–49.
[78] M. Gao, L. Zhu, C.K. Peh, G.W. Ho, Solar absorber material and system designs for photothermal water vaporization towards clean water and energy production, Energy Environ. Sci. 12 (2019) 841–864.
[79] M. Cho, H. Chung, W. Choi, J. Yoon, Linear correlation between inactivation of E. coli and OH radical concentration in TiO_2 photocatalytic disinfection, Water Res. 38 (2004) 1069–1077.
[80] G. Li, K.H. Wong, X. Zhang, C. Hu, C.Y. Jimmy, R.C.Y. Chan, P.K. Wong, Degradation of acid orange 7 using magnetic AgBr under visible light: the roles of oxidizing species, Chemosphere 76 (2009) 1185–1191.
[81] Y. Duan, M. Zhang, L. Wang, F. Wang, L. Yang, X. Li, C. Wang, Plasmonic Ag-TiO_{2-x} nanocomposites for the photocatalytic removal of NO under visible light with high selectivity: the role of oxygen vacancies, Appl. Catal. B Environ. 204 (2017) 67–77.
[82] M. Janczarek, E. Kowalska, On the origin of enhanced photocatalytic activity of copper-modified titania in the oxidative reaction systems, Catalysts 7 (2017) 317.
[83] P.L. Khoo, K. Satou, M. Izaki, The electronic states of copper oxides photoactive layers prepared by electrodeposition followed by annealing, IOP Conf. Ser. Mater. Sci. Eng. 920 (2020), 012028.
[84] P. Basnet, E. Anderson, Y. Zhao, Hybrid Cu_xO–TiO_2 nanopowders prepared by ball milling for solar energy conversion and visible-light-induced wastewater treatment, ACS Appl. Nano Mater. 2 (2019) 2446–2455.
[85] J. Hasan, H. Li, G. Tian, C. Qin, Fabrication of Cr_2S_3-GO-TiO_2 composite with high visible-light-driven photocatalytic activity on degradation of organic dyes, Chem. Phys. 539 (2020), 110950.

National Conference on
Advances in Sustainable Chemistry and Material Science
(ASCMS-2022)

ASCMS

Paper Presentation Certificate

This is to certify that

Prof./Dr./Mr./Ms. *Rajmoni Basumatary* of *Bodoland University, Kokrajhar* has made oral presentation on the topic entitled "*Broad LSPR enhanced Cu_2O/TiO_2 heterojunction photocatalyst for MB degradation*" in the National Conference on Advances in Sustainable Chemistry and Material Science-2022 held on 29th & 30th April 2022 in the Department of Chemistry, Bodoland University, Kokrajhar, Assam, India.

Prof. Laishram Ladu Singh (Vice Chancellor)	Dr. Manjil Basumatary (Chairperson)	Dr. Sanjay Basumatary (Convenor)	Dr. Dhrubajyoti Haloi (Convenor)	Dr. Hemaprabha Saikia (Convenor)

G20 भारत 2023 INDIA S20 SCIENCE 2023 INDIA

MIZORAM UNIVERSITY

Azadi Ka Amrit Mahotsav

A CENTRAL UNIVERSITY ESTABLISHED BY AN ACT OF PARLIAMENT, ACCREDITED 'A' GRADE BY NAAC (2019)

Certificate of Presentation

This certificate acknowledges that

Mr./Ms./Dr. Rajmoni Basumatary

Dept. of Physics, Bodoland University Assam

has successfully presented the paper entitled "Pushing Frontiers: Plasmonic Ag-enhanced Ni-Cr LDH Photocatalysts Propel Swift Visible Light Dye Degradation" at the International Conference on Recent Advances in Mathematical, Physical, and Chemical Sciences (ICRAMPC-2024) organized by School of Physical Sciences, Mizoram University, Aizawl during February 21-23, 2024.

Prof. Dibakar Chandra Deka
Vice-Chancellor

Prof. Suman Rai
Dean & Chairman

Prof N. Mohondas Singh
Convener